

## The Star Formation Rate of the Milky Way as seen by *Herschel*

D. ELIA,<sup>1</sup> S. MOLINARI,<sup>1</sup> E. SCHISANO,<sup>1</sup> J. D. SOLER,<sup>1</sup> M. MERELLO,<sup>2</sup> D. RUSSEIL,<sup>3</sup> M. VENEZIANI,<sup>4</sup> A. ZAVAGNO,<sup>3,5</sup> A. NORIEGA-CRESPO,<sup>6</sup> L. OLMI,<sup>7</sup> M. BENEDETTINI,<sup>1</sup> P. HENNEBELLE,<sup>8</sup> R. S. KLESEN,<sup>9,10</sup> S. LEURINI,<sup>11</sup> R. PALADINI,<sup>12</sup> S. PEZZUTO,<sup>1</sup> A. TRAFICANTE,<sup>1</sup> D. J. EDEN,<sup>13,14</sup> P. G. MARTIN,<sup>15</sup> M. SORMANI,<sup>9</sup> A. COLETTA,<sup>1,16</sup> T. COLMAN,<sup>8</sup> R. PLUME,<sup>17</sup> Y. MARUCCIA,<sup>1</sup> C. MININNI,<sup>1</sup> AND S. J. LIU<sup>1</sup>

<sup>1</sup>INAF - Istituto di Astrofisica e Planetologia Spaziali, Via Fosso del Cavaliere 100, I-00133 Roma, Italy

<sup>2</sup>Departamento de Astronomía, Universidad de Chile, Casilla 36-D, Correo Central, Santiago, Chile

<sup>3</sup>Aix Marseille Univ., CNRS, CNES, LAM, Marseille, France

<sup>4</sup>Science & Technology Corporation, Olof Palmestraat 14, 2616 LR Delft, The Netherlands

<sup>5</sup>Institut Universitaire de France, Paris, France

<sup>6</sup>Space Telescope Science Institute, 3700 San Martin Dr, Baltimore, MD 21218, USA

<sup>7</sup>INAF - Osservatorio Astrofisico di Arcetri, Largo E. Fermi 5, 50125, Firenze, Italy

<sup>8</sup>Université Paris-Saclay, Université Paris Cité, CEA, CNRS, AIM, 91191, Gif-sur-Yvette, France

<sup>9</sup>Universität Heidelberg, Zentrum für Astronomie, Institut für theoretische Astrophysik, Albert-Ueberle-Str. 2, D-69120 Heidelberg, Germany

<sup>10</sup>Universität Heidelberg, Interdisziplinäres Zentrum für Wissenschaftliches Rechnen, Im Neuenheimer Feld 205, D-69120 Heidelberg, Germany

<sup>11</sup>INAF - Osservatorio Astronomico di Cagliari, Via della Scienza 5, I-09047 Selargius (CA), Italy

<sup>12</sup>Infrared Processing Analysis Center, California Institute of Technology, Pasadena, CA 91125, USA

<sup>13</sup>Astrophysics Research Institute, Liverpool John Moores University, IC2, Liverpool Science Park, 146 Brownlow Hill, Liverpool, L3 5RF, UK

<sup>14</sup>Armagh Observatory and Planetarium, College Hill, Armagh BT61 9DB, UK

<sup>15</sup>Canadian Institute for Theoretical Astrophysics, University of Toronto, 60 St. George Street, Toronto, ON M5S 3H8, Canada

<sup>16</sup>Dipartimento di Fisica, Sapienza Università di Roma, Piazzale Aldo Moro 2, I-00185, Rome, Italy

<sup>17</sup>Department of Physics & Astronomy, University of Calgary, 2500 University Dr. NW, Calgary, AB, T2N1N4, Canada

Submitted to ApJ

## ABSTRACT

We present a new derivation of the Milky Way’s current star formation rate (SFR) based on the data of the Hi-GAL Galactic plane survey. We estimate the distribution of the SFR across the Galactic plane from the star-forming clumps identified in the Hi-GAL survey and calculate the total SFR from the sum of their contributions. The estimate of the global SFR amounts to  $2.0 \pm 0.7 \text{ M}_\odot \text{ yr}^{-1}$ , of which  $1.7 \pm 0.6 \text{ M}_\odot \text{ yr}^{-1}$  coming from clumps with reliable heliocentric distance assignment. This value is in general agreement with estimates found in the literature of last decades. The profile of SFR density averaged in Galactocentric rings is found to be qualitatively similar to others previously computed, with a peak corresponding to the Central Molecular Zone and another one around Galactocentric radius  $R_{\text{gal}} \sim 5 \text{ kpc}$ , followed by an exponential decrease as  $\log(\Sigma_{\text{SFR}}/[\text{M}_\odot \text{ yr}^{-1} \text{ kpc}^{-2}]) = a R_{\text{gal}}/[\text{kpc}] + b$ , with  $a = -0.28 \pm 0.01$ . In this regard, the fraction of SFR produced within and outside the Solar circle is 84% and 16%, respectively; the fraction corresponding to the far outer Galaxy ( $R_{\text{gal}} > 13.5 \text{ kpc}$ ) is only 1%. We also find that, for  $R_{\text{gal}} > 3 \text{ kpc}$ , our data follow a power law as a function of density, similarly to the Kennicutt-Schmidt relation. Finally, we compare the distribution of the SFR density across the face-on Galactic plane and those of median parameters, such as temperature, luminosity/mass ratio and bolometric temperature, describing the evolutionary stage of Hi-GAL clumps. We found no clear correlation between the SFR and the clump evolutionary stage.

**Keywords:** stars: formation — stars: protostars — ISM:general

## 1. INTRODUCTION

Corresponding author: Davide Elia  
 davide.elia@inaf.it

The star formation rate (SFR) is a widely used parameter to globally characterize galaxies (see [Kennicutt & Evans 2012](#), and references therein). In the absence of small-scale

description of the star forming activity in external galaxies, their SFR expresses the fundamental relationship between the stellar mass and the gas reservoir on which our understanding of galaxy formation and evolution is based (see, e.g., McKee & Ostriker 2007; Krumholz 2014).

Several estimates of the SFR have been computed for the Milky Way as well. Considering, in principle, the total mass of available molecular gas and the free-fall time in typical conditions of clouds in the Galaxy would lead to a prediction of a global SFR of  $300 \text{ M}_\odot \text{ yr}^{-1}$  (reducible to  $46 \text{ M}_\odot \text{ yr}^{-1}$  if only bound clouds are considered, Evans et al. 2021). However, the actual estimates based on direct star formation indicators converge towards a value of a few  $\text{M}_\odot \text{ yr}^{-1}$  (see Licquia & Newman 2015, and references therein). As shown by Fraser-Mckelvie et al. (2019) and Boardman et al. (2020), this is a typical SFR for galaxies with characteristics similar to those of the Milky Way, while in different galaxies values up to a few tens of  $\text{M}_\odot \text{ yr}^{-1}$  can be reached (see, e.g., Chomiuk & Povich 2011; Mutch et al. 2011).

State-of-the-art estimates of the SFR, summarized in Table 1, provide an illustration of the variations found using different methods. The previous compilation, presented in Chomiuk & Povich (2011, their Table 1), renormalized some of the archival values from the literature, to conform all of them to the same initial mass function (IMF, Kroupa & Weidner 2003; Kennicutt et al. 2009), as also recommended by Davies et al. (2011).

Misiriotis et al. (2006), using a direct relation between COBE/DIRBE 100  $\mu\text{m}$  emission and SFR already adopted for external galaxies, provided a value of  $2.7 \text{ M}_\odot \text{ yr}^{-1}$  for the Milky Way's SFR. Robitaille & Whitney (2010) estimated a SFR from  $0.68$  to  $1.45 \text{ M}_\odot \text{ yr}^{-1}$ , starting from young stellar objects (YSOs) revealed in the *Spitzer*/IRAC GLIMPSE Galactic plane survey, and using model spectral energy distributions (SEDs) to predict the brightness and color of the synthetic YSOs at different wavelengths.

More recent results do not use new data sets, but are derived by reconsidering values existing in the literature: Chomiuk & Povich (2011) determine a SFR of  $1.9 \pm 0.4 \text{ M}_\odot \text{ yr}^{-1}$  by combining and re-normalizing literature results from 1978 to 2011. Licquia & Newman (2015) derived a SFR of  $1.65 \pm 0.19 \text{ M}_\odot \text{ yr}^{-1}$  by statistically combining the prior measurements of this quantity in the literature through a hierarchical Bayesian method.

An independent estimate of the SFR can be given through a technique which uses far-infrared *Herschel*<sup>1</sup> satellite (Pilbratt et al. 2010) data, and in particular photometric observations carried out by its PACS (at 70 and 160  $\mu\text{m}$ ,

Poglitsch et al. 2010) and SPIRE (at 250, 350 and 500  $\mu\text{m}$ , Griffin et al. 2010) cameras. Veneziani et al. (2013) developed such method that starts from the compact sources detected in *Herschel* maps. They generally correspond to unresolved clumps that already host active star formation, or, alternatively, are starless but show conditions for future activity. By considering the former category of sources, Veneziani et al. (2013) evaluated the contribution of each individual clump to the total SFR in two  $2^\circ \times 2^\circ$ -tiles of Hi-GAL (*Herschel* InfraRed Galactic Plane Survey, Molinari et al. 2010), namely the Open Time Key Project for unbiasedly surveying the whole Galactic plane with PACS and SPIRE. For comparison, they also derived the SFR of the same two regions through the method of Li et al. (2010) based on assuming a direct relation between SFR and 70  $\mu\text{m}$  emission. Subsequently, by assuming that these two fields are representative of the entire Milky Way, Noriega-Crespo (2013) extrapolated for the entire Galactic SFR an estimate of  $2.1 \pm 0.4 \text{ M}_\odot \text{ yr}^{-1}$ .

Other works also discussed the profile of the Milky Way SFR as a function of the Galactocentric distance  $R_{\text{gal}}$ , both to quantify the ability of different zones of our Galaxy to form stars, and to make a comparison with external galaxies, for which this relation is observed. A typical approach is to study the SFR density, averaged in concentric Galactic rings, as a function of the middle radius of the ring (e.g., Guesten & Mezger 1982; Portinari & Chiosi 1999; Kennicutt & Evans 2012; Lee et al. 2016). It is generally seen that the profile of this quantity has an absolute maximum in correspondence of the Central Molecular Zone (CMZ), another local maximum around at  $R_{\text{gal}} \sim 4 - 5 \text{ kpc}$  (with a dip in the middle, centered at  $R_{\text{gal}} \sim 2 \text{ kpc}$ ), and an exponential decrease at larger radii.

In this paper, by extending the method of Veneziani et al. (2013), refined by Veneziani et al. (2017), to the clump catalog of the entire Hi-GAL survey, we present a direct and self-consistent estimate of the SFR for the whole Milky Way, illustrating both the global SFR and its distribution across the Galactic plane.

In Section 2 we show how Hi-GAL protostellar clump properties can be used to obtain an estimate of the current Galactic SFR. In Section 3 we discuss how the SFR is distributed across the Milky Way, adopting both the  $[\ell, b]$  and the pole-on perspective. We also make a test of the Kennicutt-Schmidt law with our data, and investigate possible links between local SFR and clump average evolutionary stage. Finally, in Section 4 we draw our conclusions.

## 2. THE HERSCHEL-BASED MILKY WAY'S SFR ESTIMATION

### 2.1. Source selection

<sup>1</sup> *Herschel* is an ESA space observatory with science instruments provided by European-led Principal Investigator consortia and with important participation from NASA.

**Table 1.** Star formation rate (SFR) estimates for the Milky Way

Method	SFR $M_{\odot} \text{ yr}^{-1}$	Reference
Ionization rate from radio free-free	0.35 <sup>a</sup>	Smith et al. (1978)
Ionization rate from radio free-free	$2.0 \pm 0.6^a$	Guesten & Mezger (1982)
Ionization rate from radio free-free	$1.6 \pm 0.5^a$	Mezger (1987)
Ionization rate from [N II] 205 $\mu\text{m}$ (COBE)	$2.6 \pm 1.3^a$	Bennett et al. (1994)
Ionization rate from [N II] 205 $\mu\text{m}$ (COBE)	$2.0 \pm 1.0^a$	McKee & Williams (1997)
O/B Star Counts	$1.8 \pm 0.6^a$	Reed (2005)
Nucleosynthesis from $^{26}\text{Al}$ (INTEGRAL)	$2.0 \pm 1.2^a$	Diehl et al. (2006)
Continuum emission at 100 $\mu\text{m}$ (COBE)	$1.9 \pm 0.8^a$	Misiriotis et al. (2006)
Ionization rate from microwave free-free (WMAP)	$2.4 \pm 1.2^a$	Murray & Rahman (2010)
YSO counts ( <i>Spitzer</i> )	$1.1 \pm 0.4^a$	Robitaille & Whitney (2010)
YSO counts (MSX)	$1.8 \pm 0.3$	Davies et al. (2011)
Combination of literature values	$1.9 \pm 0.4$	Chomiuk & Povich (2011)
Continuum emission at 70 $\mu\text{m}$ ( <i>Herschel</i> )	$2.1 \pm 0.4$	Noriega-Crespo (2013)
Combination of literature values	$1.65 \pm 0.19$	Licquia & Newman (2015)
FIR clump counts ( <i>Herschel</i> )	$2.0 \pm 0.7$	This work

<sup>a</sup>This value is not taken from the original article, but was re-scaled by Chomiuk & Povich (2011) to normalize all literature results to the same IMF (see text).

We calculated the Galactic SFR using the physical properties of clumps identified in the Hi-GAL survey (Elia et al. 2021). These objects were identified and cataloged as follows.

The detection and 5-band photometry of Hi-GAL compact sources (i.e. unresolved or poorly resolved) were performed through the CuTEx algorithm (Molinari et al. 2011) in the five Hi-GAL bands, to obtain the single-band catalogs presented by Molinari et al. (2016) and Molinari et al. (in prep.).

Starting from these lists, Elia et al. (2021) obtained a band-merged catalog, from which only spectral energy distributions (SEDs) with a shape eligible for a modified black body fit in the range from 160 to 500  $\mu\text{m}$  were selected (further details can be also found in Elia et al. 2013, 2017).

Heliocentric distances were estimated by Mège et al. (2021) in three steps: *i*) by extracting the most reliable velocity component along the line of sight from available spectroscopic surveys of the Galactic plane; *ii*) by applying the rotation curve of Russeil et al. (2017) and solving the near/far distance ambiguity towards the inner Galaxy by considering H $\alpha$  absorption; and *iii*) by complementing this information with independent estimates such as H $\alpha$  region distances or maser parallaxes. The medians of the absolute and relative error on distances of Mège et al. (2021) are 0.54 kpc and 16%, respectively.

As pointed out in Elia et al. (2017, 2021), the Hi-GAL compact sources are distributed along a wide range of heliocentric distances and consequently achieve a variety of physical sizes corresponding to different kinds of structures: from

single cores to larger overdensities hosting a more complex but unresolved morphology. In particular, the majority of Hi-GAL sources fulfill the definition of clump based on physical diameter ( $0.3 < D < 3$  pc, Bergin & Tafalla 2007).

As a rough criterion to classify the clumps in star forming vs quiescent (designated for brevity as protostellar and starless, respectively), Elia et al. (2021) adopted the availability/lack of a detection at 70  $\mu\text{m}$ , respectively.

The modified black body fit provided temperatures for the clump SEDs and, for cases with an available distance estimate, also the mass and the bolometric luminosity. The mass was used to further classify the starless clumps as gravitationally bound (called pre-stellar) vs unbound, by using a gravitational stability criterion based on the so-called third Larson's relation (Larson 1981). For pre-stellar sources the luminosity was estimated from the whole integral of the best-fitting modified black body. For protostellar sources, generally showing an excess of emission at  $\lambda < 70 \mu\text{m}$  with respect to the modified black body (e.g., Dunham et al. 2008; Giannini et al. 2012; Elia et al. 2017), the luminosity is estimated by considering the sum of the integrals of the observed SED for  $\lambda < 160 \mu\text{m}$  and of the best-fitting modified black body for  $\lambda \geq 160 \mu\text{m}$ , respectively.

The same considerations made above about the physical size can be extended to the other distance-dependent observables mass and luminosity. Their ranges of variability extend over several orders of magnitude not only due to intrinsic differences among objects (that can be appreciated among sources located at the same distance), but also - and above

all - due to the wide range of underlying distances, as figures 9 and 13 of [Elia et al. \(2021\)](#) clearly illustrate. More quantitatively, 99% of Hi-GAL clumps of [Elia et al. \(2021\)](#) provided with a distance estimate have masses ranging from 0.1 to  $10^4 M_{\odot}$ , and luminosities ranging from 0.1 to  $10^5 L_{\odot}$ .

To compute the SFR through the method described in Section 2.2, first we consider all 29880 protostellar clumps provided with a heliocentric distance. Subsequently, in Section 2.2.1 we evaluate and suggest a reasonable additional term which accounts for the contribution by further 5532 protostellar clumps lacking a distance determination.

## 2.2. Computation of the SFR

To determine the SFR we followed the method described by [Veneziani et al. \(2013\)](#) and refined by [Veneziani et al. \(2017\)](#).

In short, the contribution of each protostellar source to the total SFR is computed through theoretical evolutionary tracks reported in the bolometric luminosity vs mass diagram ([Molinari et al. 2008; Baldeschi et al. 2017a; Elia et al. 2021](#)). At each time step, together with the clump mass-luminosity pair, the mass of the internal protostar being formed is also computed. At the end point of the theoretical track both the final mass of the star and the corresponding total elapsed time are known. The ratio between these two quantities constitutes the SFR contribution from the given clump.

The evolutionary tracks were initially obtained by [Molinari et al. \(2008\)](#) for the case of an object forming a single central star but, especially at higher masses, we actually deal with clumps possibly hosting the formation of entire protoclusters (e.g. [Baldeschi et al. 2017b](#)). [Veneziani et al. \(2017\)](#) took into consideration this aspect by applying a Monte Carlo procedure to an evolutionary model of turbulent cores to account for the wide multiplicity of sources produced during the clump collapse. We implemented this refinement in this work as well (for details, see [Veneziani et al. 2017](#)).

Furthermore, given the wide range of clump heliocentric distances quoted in the Hi-GAL catalog ([Elia et al. 2017, 2021](#)), a distance bias might be expected to affect the estimate of physical parameters for these objects. [Baldeschi et al. \(2017b\)](#) proposed a method to evaluate this possible bias by simulating the appearance of nearby star forming regions observed by the *Herschel* Gould Belt Survey ([André et al. 2010](#)) if they were moved to larger distances (from 0.75 to 7 kpc), comparable to those typically found in the Hi-GAL survey. Subsequently, in [Baldeschi et al. \(2017a\)](#) this approach was applied, in particular, to the estimation of the SFR. For three nearby regions they compared the SFR obtained from YSO counts (based on an updated version of Equation 1 of [Lada et al. 2010](#)) to that estimated through

the method of [Veneziani et al. \(2017\)](#) from the clumps detected in the *Herschel* maps “displaced” at different virtual distances. They found that the two estimates remain consistent with each other within a factor 2 at various probed distances.

Based on these premises we feel confident to adopt the method of [Veneziani et al. \(2017\)](#). As mentioned above, the output of the algorithm we used is the contribution of each clump  $\Sigma_{\text{cl}}$  to the global SFR. This quantity depends on the evolutionary track in the  $L/M$  plot, which, in turn, is defined by the initial clump mass  $M_{\text{cl}}$ . Although not explicitly stated in the original articles, this algorithm associates the final star mass to the input clump mass by interpolating the locus of final masses of known evolutionary tracks with a power law. Here we explicitly report the corresponding formula we used:

$$\text{SFR}_{\text{cl}} = (5.6 \pm 1.4) \times 10^{-7} (M_{\text{cl}}/M_{\odot})^{0.74 \pm 0.03} M_{\odot} \text{ yr}^{-1}. \quad (1)$$

We propose this relation hereafter as an operational prescription for an immediate application of the method of [Veneziani et al. \(2017\)](#).

The global SFR, estimated by adding up all these contributions, amounts to  $1.7 \pm 0.6 M_{\odot} \text{ yr}^{-1}$ . The uncertainty is given by the error propagation, combining in quadrature the uncertainties affecting the clump masses and the parameters appearing in Equation 1.

Adopting a classification of inner vs outer Galaxy delimited by the Solar circle with a radius of 8.34 kpc (as in [Mège et al. 2021; Elia et al. 2021](#)), it is possible to give separately the contributions to the global SFR from these two zones: 1.5 (i.e. the 84% of the total) and  $0.3 M_{\odot} \text{ yr}^{-1}$  (16%), respectively.

### 2.2.1. Contribution from sources devoid of a distance estimate

It is to notice that the SFR estimate reported above should be intended as a lower limit, since the input data, namely the protostellar clump list, is incomplete for the reasons described in the following. First, since the mass completeness in the Hi-GAL catalog is a function of the heliocentric distance ([Elia et al. 2017](#)), faint and/or far and/or cold protostellar clumps might remain undetected at all. We address this issue in Appendix A. Second, protostellar clumps undetected at  $70 \mu\text{m}$  (for the same reasons written above), but detected at the other ones, result misclassified as starless and are not involved in the SFR calculation. In fact, in the literature examples can be found of spectroscopic signatures of active star formation detected in  $70 \mu\text{m}$ -dark clumps (e.g., [Traficante et al. 2017](#)). Third, 5532 sources classified as protostellar in the Hi-GAL catalog are not provided with a distance, and consequently not involved in our previous calculation (see Figure 1).

Regarding the last point, it is possible to give an estimate of the missing contribution from this subsample by simulating a

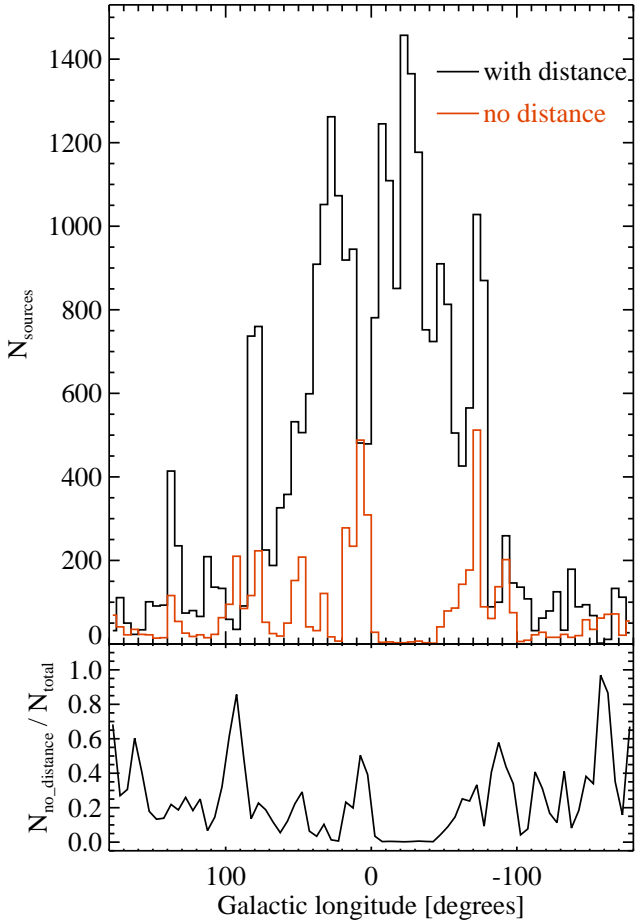


**Figure 1.** *Top*: distributions of Hi-GAL protostellar clumps with and without a heliocentric distance estimate (black and red histograms, respectively) in  $5^\circ$ -wide bins of Galactic longitude. *Bottom*: number ratio between protostellar clumps without a distance estimate and the total number, in the same longitude bins as in the top panel.

plausible realization of distances for sources whose distance is unknown. In this way, masses can be obtained also for them, to be inputted in the SFR calculation.

We simulated a set of 5532 distances whose distribution follows the one of the protostellar sources provided with a distance estimate. Then we randomly assigned each simulated distance to a clump devoid of distance, computed mass and luminosity accordingly, and estimated the contribution to the SFR with the usual procedure. This random assignment of distances to clumps has been repeated 100 times (two of which are shown in Figure 2), to keep safe from specific effects possibly induced by a single realization. The 100 corresponding estimates of additional SFR contribution are found to be confined in the relatively narrow range  $0.20$  to  $0.23 \text{ M}_\odot \text{ yr}^{-1}$ , with an average of  $0.22 \text{ M}_\odot \text{ yr}^{-1}$  and a standard deviation of  $0.01 \text{ M}_\odot \text{ yr}^{-1}$ . Notice that this standard deviation is expected to decrease by increasing the number of simula-

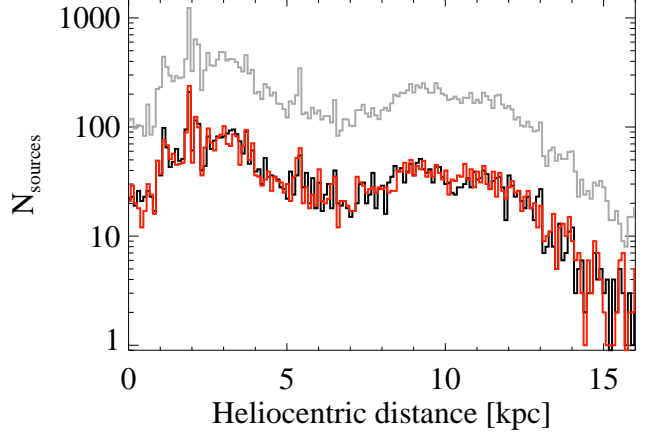


**Figure 2.** Two examples (black and red histograms, respectively, in bins of  $100 \text{ pc}$ ) of realizations of heliocentric distance distributions to be assigned, as a test, to Hi-GAL protostellar clumps devoid of a distance estimate, compared with the distance distribution for sources provided with a distance estimate (gray histogram, Elia et al. 2021).

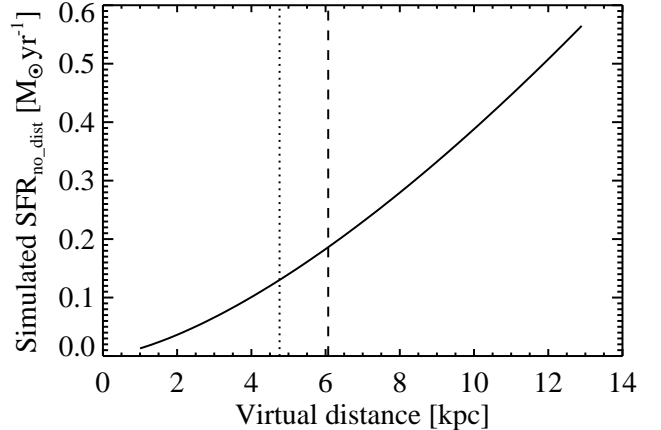


**Figure 3.** Probable contribution to the overall SFR from sources lacking a distance estimate if they were all located at the same virtual distance. The dotted and dashed lines represent the median and the average of the real distance distribution, respectively.

tion as desired. The real uncertainty, instead, is dominated by the typical error bar associated to the SFR contribution evaluated for each simulation, which is  $0.08 \text{ M}_\odot \text{ yr}^{-1}$ .

In conclusion, a reasonable estimate of the total Galactic SFR taking into account the correction calculated above is  $2.0 \pm 0.7 \text{ M}_\odot \text{ yr}^{-1}$ .

The above test is based on the assumption that the real (unknown) distances of sources lacking this information follow the same distribution of the known ones. However, the lack of a distance estimate, i.e. the impossibility of individuating a clear and/or reliable spectral component along the line of sight of the Hi-GAL source (Mège et al. 2021), could be, in principle, due to specific local conditions. This could then

produce a departure from the assumed behavior of distance distributions. In this respect, the most unfavorable hypothetical case would be to have all sources located at the same distance. Therefore, supposing that all sources without distance were located at a minimum and at a maximum distance, respectively, helps us to identify a range of maximum variability of their contribution to the total SFR. We therefore analyzed the behavior of such contribution for a common distance varying between 1 and 13 kpc (these limits are suggested by the distributions shown in Figure 2). From Figure 3 we see that for a virtual common distance of 1 kpc the contribution to the SFR would be negligible, while for 13 kpc it would amount to  $0.57 \text{ M}_\odot \text{ yr}^{-1}$ . Clearly, both scenarios (and, consequently, the corresponding contributions to SFRs) are unrealistic, but this test proves that, even in case of an extremely unfavorable distance distribution of clumps without distance assignment, the order of magnitude of the SFR increment estimated through our test would be confirmed. Finally, we notice that, assuming that all sources without known distance were placed at the median and the average of the known distance distribution, their contribution would amount to  $0.13$  and  $0.19 \text{ M}_\odot \text{ yr}^{-1}$ , respectively (see Figure 3).

A final test we propose consists in a hybrid approach between the two followed above. Indeed, the top panel of Figure 1 suggests that the distribution in longitude of clumps lacking a distance assignment is far from being uniform and, moreover, it does not strictly follow the behavior of sources with a distance (as testified by the high degree of scatter of the ratio between the former distribution and the overall one, shown in the bottom panel). Statistically significant amounts of sources without a distance are found in correspondence of the innermost Galactic longitudes ( $0^\circ \lesssim \ell \lesssim 20^\circ$ ), and in the direction of the Carina arm ( $270^\circ \lesssim \ell \lesssim 310^\circ$ ). The first case can be treated with relative ease, by arbitrarily placing all the sources without distance and with  $|\ell| < 20^\circ$  at the Galactic center distance of 8.34 kpc, and proceeding for the remaining sources by simulating distances distributed as the known ones. In this case, the additional term to the global SFR would amount to  $0.17 \pm 0.06 \text{ M}_\odot \text{ yr}^{-1}$ .

### 2.3. Comparison with the previous literature

Adopting the value of  $2.0 \pm 0.7 \text{ M}_\odot \text{ yr}^{-1}$  as our final estimate for the Milky Way SFR, and comparing with values in Table 1, it can be seen that it is consistent, within the error bars, with all but one (namely Smith et al. 1978) estimates collected and normalized by Chomiuk & Povich (2011), and with the estimates of Chomiuk & Povich (2011) themselves and of Licquia & Newman (2015). Remarkably, our estimate is also perfectly consistent, within the errors, with that of Noriega-Crespo (2013), confirming that his choice to extrapolate the SFR estimate from an area of 8 sq. deg. to the entire 720 sq. deg was quite reasonable.

Our result, in essence, corroborates the common idea - supported by the fact that a variety of approaches leads to similar values - that the current SFR of the Milky Way lies in the range  $1.5\text{--}2.5 \text{ M}_\odot \text{ yr}^{-1}$ , which is consistent with the values found for spiral galaxies (e.g., Kennicutt & Evans 2012).

## 3. THE SFR ACROSS THE GALACTIC PLANE

We studied the SFR distribution across the Galactic Plane. From here on, we will only consider the contribution to SFR given by clumps whose heliocentric distance is known, for which the position in the Galaxy can be determined.

### 3.1. Mapping SFR in Galactic coordinates: the Central Molecular Zone

A first view of SFR distribution in the Galactic plane can be given in the  $[\ell, b]$  plane, as shown in Figure 4, top. It can be seen that, approximately, most of the total SFR (90%) comes from the inner  $120^\circ$  (Figure 4, bottom).

For the used binning of  $3^\circ$  in longitude and  $0.2^\circ$  in latitude, the three most prominent local maxima are found in pixels corresponding to the ranges  $336^\circ < \ell < 339^\circ$  and  $-0.2^\circ < b < 0.0^\circ$  (containing the G337.3420.119 region, Jackson et al. 2018),  $27^\circ < \ell < 30^\circ$  and  $0.0^\circ < b < 0.2^\circ$ , and  $18^\circ < \ell < 21^\circ$  and  $-0.2^\circ < b < 0.0^\circ$ , respectively.

Through the  $[\ell, b]$  view of the Galactic SFR it is also possible to make a direct comparison with SFRs estimated in the literature for the CMZ, generally taken as a rectangular coordinate box in such plane. In Table 2 we report a list of recent  $\text{SFR}_{\text{CMZ}}$  estimates, each of them derived in a different area around the Galactic center, and the output of our method for the same area.

We found a good agreement with the  $\text{SFR}_{\text{CMZ}}$  estimates reported in Crocker et al. (2011) and Immer et al. (2012). We also found a fairly good agreement with Barnes et al. (2017) on  $\text{SFR}_{\text{CMZ}}$ , which those authors estimated from monochromatic fluxes or bolometric luminosities available in the literature from 1998 to 2011, and ranging from  $0.07$  to  $0.12 \text{ M}_\odot \text{ yr}^{-1}$ , to be compared with our estimate of  $0.06 \pm 0.02 \text{ M}_\odot \text{ yr}^{-1}$ .

Our results, however, appear to disagree with the SFR estimated for the CMZ in Yusef-Zadeh et al. (2009) and Longmore et al. (2013). The  $\text{SFR}_{\text{CMZ}}$  in Yusef-Zadeh et al. (2009) is above our result, which is most likely due to an excessive number of early YSOs involved in the calculation, as discussed in Koepferl et al. (2015), who quantify this overestimate in a factor of 3. Correcting by this factor, the estimate of Yusef-Zadeh et al. (2009) would turn out to be consistent with our value ( $0.04 \pm 0.02 \text{ M}_\odot \text{ yr}^{-1}$ ) within the uncertainties.

Longmore et al. (2013) estimated  $\text{SFR}_{\text{CMZ}} = 0.035 \text{ M}_\odot \text{ yr}^{-1}$  in the range  $2.5^\circ < \ell < 3.5^\circ$  and  $|b| < 0.5^\circ$ , and  $0.06 \text{ M}_\odot \text{ yr}^{-1}$  if the wider latitude range  $|b| < 1^\circ$  is considered in the central  $|\ell| < 1^\circ$ . Correspondingly, we calculate  $\text{SFR}_{\text{CMZ}} = 0.11$  and  $0.12 \text{ M}_\odot \text{ yr}^{-1}$  for these two zones,

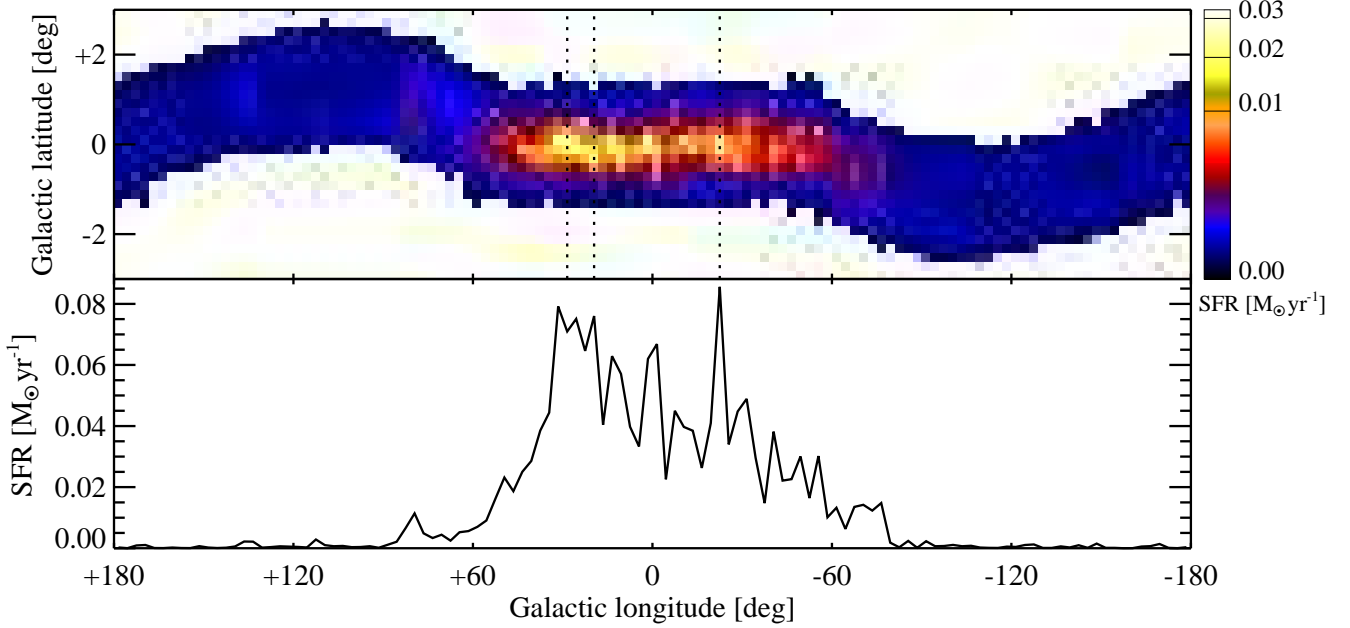


**Figure 4.** *Top:* Star formation rate (SFR) toward the Galactic plane in  $3^\circ \times 0.2^\circ$  bins in Galactic longitude and latitude, respectively. It is to notice that in the outer Galaxy the Hi-GAL latitude coverage follows the variations in the midplane position, or Galactic warp (Westerhout 1957). For a better rendering of the image dynamic range, the color scale follows a power law with exponent 0.4. The dotted lines indicate the location of the three most prominent SFR peaks. *Bottom:* SFR as a function of longitude, estimated from the sum of the results reported in the top panel across Galactic latitude.

**Table 2.** Star formation rate estimates for the Central Molecular Zone

Method	Area boundaries	SFR <sub>CMZ</sub> (lit.)	Reference	SFR <sub>CMZ</sub> (this work)
		$M_\odot \text{ yr}^{-1}$		$M_\odot \text{ yr}^{-1}$
YSO counts ( <i>Spitzer</i> )	$ \ell  < 1^\circ,  b  < 10'$	0.14	Yusef-Zadeh et al. (2009)	$0.04 \pm 0.02$
Continuum emission at 60, 100 $\mu\text{m}$ (IRAS)	$ \ell  < 3^\circ,  b  < 1^\circ$ <sup>a</sup>	0.12	Crocker et al. (2011)	$0.12 \pm 0.05$
Continuum emission at 60, 100 $\mu\text{m}$ (IRAS)	$ \ell  < 0.8^\circ,  b  < 0.3^\circ$	0.08	Crocker et al. (2011)	$0.04 \pm 0.02$
YSO counts ( <i>Spitzer</i> )	$ \ell  < 1.5^\circ,  b  < 0.5^\circ$	0.08	Immer et al. (2012)	$0.08 \pm 0.03$
Ionization rate from radio free-free	$2.5^\circ < \ell < 3.5^\circ,  b  < 0.5^\circ$	0.035	Longmore et al. (2013)	$0.11 \pm 0.04$
Ionization rate from radio free-free	as above, but $ b  < 1^\circ$ for $ \ell  < 1^\circ$	0.06	Longmore et al. (2013)	$0.12 \pm 0.05$
Continuum emission at 24 $\mu\text{m}$ ( <i>Spitzer</i> )	$ \ell  < 1^\circ,  b  < 0.5^\circ$	$0.09 \pm 0.02$	Barnes et al. (2017) <sup>b</sup>	$0.06 \pm 0.02^c$
Continuum emission at 70 $\mu\text{m}$ ( <i>Spitzer</i> )	$ \ell  < 1^\circ,  b  < 0.5^\circ$	$0.10 \pm 0.02$		
Cont. emission at 5.8-500 $\mu\text{m}$ ( <i>Spitzer, Herschel</i> )	$ \ell  < 1^\circ,  b  < 0.5^\circ$	$0.09 \pm 0.03$		

<sup>a</sup>Differently from other rectangular areas quoted in the table, this one has an elliptical shape with axes aligned along  $\ell$  and  $b$ , and semi-axes of  $3^\circ$  and  $1^\circ$ , respectively.

<sup>b</sup>In Barnes et al. (2011), their Table 2, a further list of SFR<sub>CMZ</sub> estimates derived within the same area from monochromatic fluxes or bolometric luminosities available in the literature from 1998 to 2011 are quoted (see text). We omit them in this table for the sake of brevity.

<sup>c</sup>The three SFR<sub>CMZ</sub> estimates by Barnes et al. (2017) are derived within the same area in the sky through different methods; obviously, for the same area we can provide only one estimate.

respectively. The former one is about 3 times larger than that of Longmore et al. (2013), and not compatible with it within the associated error bar. Of course, the estimate of Longmore et al. (2013) is also the lowest among the esti-

mates from the literature collected in Table 2. The authors indeed suggest that the choice of the assumed IMF, which did not account for possible peculiar conditions of the CMZ, could affect this estimate down to a factor 1/3.

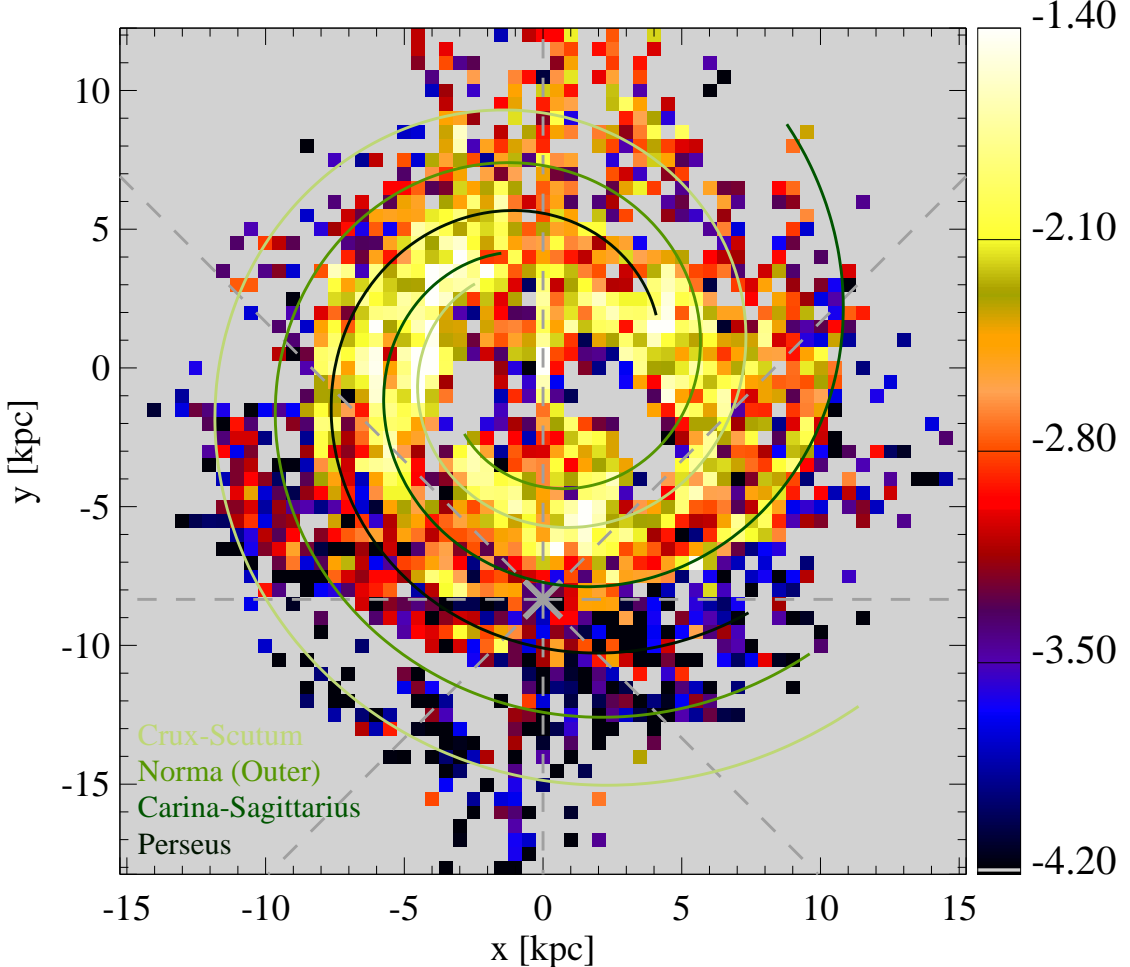


**Figure 5.** Map of the decimal logarithm of SFR density (divided by  $M_{\odot} \text{ yr}^{-1} \text{ kpc}^{-2}$ ), across the Galactic plane. The spatial bins are of  $0.5 \times 0.5 \text{ kpc}^2$ , so that the absolute SFR inside each pixel can be obtained by exponentiating the displayed logarithm, and then multiplying by a factor  $4 \text{ kpc}^2$ . The Galactic center is at the  $[0,0]$  position, while the gray X symbol indicates the position of the Sun. Gray dashed lines mark Galactic octants. Four spiral arms according to the prescription of Hou et al. (2009) are overplotted with four different tones of green; the correspondence between arms and colors is explained in the legend at the bottom left corner.

### 3.2. SFR Galactocentric profile

Using the information about the heliocentric distance, a pole-on view of SFR density in the Milky Way, mapped on a grid of  $0.5 \times 0.5 \text{-kpc}^2$  pixels, can be built. This is a simplified 2-D representation of the Galactic disk which has a structure along the third dimension, an idea of which can be taken from Figure 4. The design of the Hi-GAL survey took into account the warp of far-infrared emission already observed by IRAS towards the outer Galaxy, which however is less prominent than the Galactic warp observed in atomic gas (Westerhout 1957; Soler et al. 2022), corresponding to Galactocentric distances not achieved by objects in our sample ( $R_{\text{gal}} \gtrsim 16 \text{ kpc}$ , Voskes & Butler Burton 2006).

In Figure 5 one can appreciate that, with respect to the Galactic center (to which we assign the  $[0,0]$  position), the SFR shows a certain degree of circular symmetry.

It makes sense, therefore, to analyze the behavior of the SFR density  $\Sigma_{\text{SFR}}$ , averaged in concentric 500-pc wide rings, vs the Galactocentric radius  $R_{\text{gal}}$ . In Figure 6, top panel, a peak corresponding to the inner circle<sup>2</sup> is followed by a

<sup>2</sup> To correctly compare this plot with Figure 5, it must be considered that in this case the SFR density is obtained by dividing by the ring area, proportional to  $R_{\text{gal}}^2$ , while in Figure 5 the denominator consists of a local area extending over  $0.25 \text{ kpc}^2$ . Also notice that, as discussed in Section 2.2.1, the distribution in longitude of sources without a distance assignment shows a remarkable concentration at  $0^\circ \lesssim \ell \lesssim 20^\circ$ . Assigning the distance of the Galactic center to all of them would turn out in an even higher value for this peak.

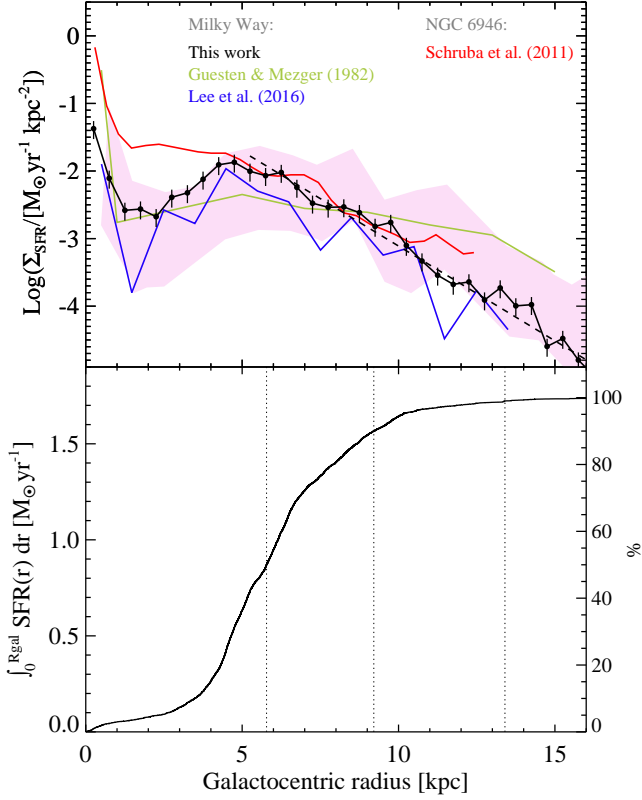


**Figure 6.** *Top:* Star formation rate (SFR) density profile estimated from the Hi-GAL observations in 0.5-kpc-wide concentric rings around the Galactic center, shown in black filled circles. Fitting the relation in Eq. 2 to the portion at  $R_{\text{gal}} \geq 5$  kpc gives  $a = -0.28 \pm 0.01$  and  $b = -0.30 \pm 0.16$ . The fit is plotted as a black dashed line. The green line shows the results of the visible-band observations considered in Guesten & Mezger (1982), re-scaled by Kennicutt & Evans (2012) to the total SFR of  $1.9 M_{\odot} \text{ yr}^{-1}$  reported in Chomiuk & Povich (2011). The blue line corresponds to the estimates obtained in Lee et al. (2016) by combining YSO NIR photometry and cloud properties from millimeter line observations. The red line shows the SFR profile of the galaxy NGC 6946, presented in Schruba et al. (2011) and adapted by Kennicutt & Evans (2012). The pink-shaded area is the region occupied by the models of Evans et al. (2022). *Bottom:* Cumulative SFR profile as a function of the Galactocentric radius, also expressed as a percentage with respect to the total SFR (y-axis on the right-hand side). The vertical dotted lines indicate, from left to right, the Galactocentric radii corresponding to 50%, 90%, and 99% of the total SFR, respectively.

wide dip between 1 and 4 kpc, mostly due to shortage of sources at these Galactocentric distances (Elia et al. 2021). This is seen also in other works (see below), and is due in part to the lack of SFR data in two lobes extending southwest and south-east of the Galactic center position over an extent of about 4 kpc (recognizable as inner void areas in Figure 5), which can not be populated with heliocentric distances since the observed clump velocities are forbidden by the adopted rotation curve (Russeil et al. 2017). In particu-

lar, in these areas absolute values of radial velocity are expected to be larger than  $100 \text{ km s}^{-1}$  (Ellsworth-Bowers et al. 2015, their Fig. 1), while most of sources observed in the corresponding longitude ranges show lower values. The kinematics of the Milky Way along these lines of sight is indeed generally dominated by the Galactic bar (Binney et al. 1991; Ellsworth-Bowers et al. 2015; Li et al. 2016). As explained by Mège et al. (2021) and Elia et al. (2021), only in cases of small deviations, the distance of the corresponding tangent point is assigned to sources, which can therefore be involved in the calculation of the SFR. Additionally, in the longitude range corresponding to the void lobe in the fourth quadrant, Mège et al. (2021) found a relatively high occurrence of noise in the original spectral survey data which in many cases prevented an estimation of the radial velocity and hence of the kinematic distance. In any case, since the two void areas are oriented approximately along Galactocentric radial directions, their influence is distributed over a certain number of rings (and therefore attenuated).

The dip in the SFR density profile is followed by another local peak at around 5 kpc. A peak in this position was predicted by Krumholz & McKee (2005) as a consequence of the distribution of the molecular gas surface density, and was found also by Portinari & Chiosi (1999) and Chiappini et al. (2001), but at  $\sim 4$  kpc. It should correspond to the so-called Molecular Ring (which is, more realistically, an effect of spiral arm arrangement, see Dobbs & Burkert 2012; Roman-Duval et al. 2016; Miville-Deschénes et al. 2017), but it does not mirror exactly the peak of source number distribution found by Elia et al. (2017) at  $R_{\text{gal}} \simeq 6$  kpc. Finally, at larger distances,  $\Sigma_{\text{SFR}}$  definitely shows a systematic decrease.

This global behavior is qualitatively similar to those shown by Kennicutt & Evans (2012) (starting from the data of Guesten & Mezger 1982) and Lee et al. (2016): an absolute maximum corresponding to the CMZ, followed by a local minimum and by another local peak at  $R_{\text{gal}} = 1$  and 5 kpc, respectively, with a decreasing behavior at larger Galactocentric distances. This general behavior was successfully modeled by Evans et al. (2022) by taking into account *i*) a dependence of the conversion factor from CO luminosity to cloud mass on metallicity (which in turn depends on  $R_{\text{gal}}$ ), and *ii*) a dependence of the star formation efficiency on the virial parameter. The envelope of the six models produced by Evans et al. (2022, their Fig. 3) in the  $\Sigma_{\text{SFR}}$  vs  $R_{\text{gal}}$  diagram delimits a belt (with a vertical width of 1-2 dex) in which the curve observed by Lee et al. (2016) is contained. Being the latter quite similar to ours in many points (Figure 6, top), a similar consistency is expected also for our data. In fact, our  $\Sigma_{\text{SFR}}$  curve is found, in turn, to be enclosed within the region occupied by the models of Evans et al. (2022), running closer to the top of it around the  $R_{\text{gal}} \simeq 5$  kpc peak, and to the

bottom of it at larger Galactocentric distances, in the range corresponding to the final decrease.

It is also important to compare the SFR profile found for Milky Way with that of external galaxies, to examine if some macroscopic bias is introduced when observing the Galaxy from the inside, rather than as a whole from the outside. The SFR Galactocentric profile of NGC 6946 galaxy obtained by Schruba et al. (2011) and adapted by Kennicutt & Evans (2012) shows, in turn, a qualitatively similar, but flatter behavior. More recently, Logroño-García et al. (2019), using H $\alpha$  emission, estimated for NGC 3994 and NGC 3995 SFR profiles which, although not quantitatively similar to that of the Milky Way, again broadly follow the same sequence of peaks and dips. Interestingly, an similar inner dip was also found by Lian et al. (2018) to be typical of local massive star-forming galaxies ( $10.5 < \log(M/M_\odot) < 11$ ).

Returning to SFR density profile of the Milky Way and to its decrease for  $R_{\text{gal}} \gtrsim 5$  kpc, Misiriotis et al. (2006) found a good agreement between the radial profile of SFR density collected from the literature and their model of spatial distribution of dust, stars, and gas in the Milky Way, constrained through COBE/DIRBE data. Such model has a functional form

$$\log(\Sigma_{\text{SFR}}/[\text{M}_\odot \text{ yr}^{-1} \text{ kpc}^{-2}]) = a R_{\text{gal}}/[\text{kpc}] + b, \quad (2)$$

with  $a \sim -0.14$ . Fitting the same relation to our data for  $R_{\text{gal}} \geq 5$  kpc, we obtain  $a = -0.28 \pm 0.01$  (Figure 6, top).

The linear fit in the same range of Galactocentric distance for the Guesten & Mezger (1982) has a much shallower slope ( $a = -0.11 \pm 0.02$ ), while the more recent curve of Lee et al. (2016), which shows more scattering, has a slope consistent with ours:  $a = -0.25 \pm 0.05$ . Finally, in the NGC 6946 case the slope shows an intermediate behavior ( $a = -0.20 \pm 0.01$ ).

The slope of -0.28 corresponds to an exponential scale length of 1.55 kpc, which is considerably shorter than those typically found for the stellar count profile in the Galactic thin disk, e.g., 2.15 kpc by Licquia & Newman (2015), 2.6 kpc by Bland-Hawthorn & Gerhard (2016, see also further references therein), and 2.2 kpc by Xiang et al. (2018). However more recently, by using LAMOST (Cui et al. 2012; Deng et al. 2012) Data Release 4, and Gaia Data Release 2 (Gaia Collaboration et al. 2018; Lindegren et al. 2018), Yu et al. (2021) derived shorter scale lengths. In particular, they considered separately stellar populations characterized by different chemical abundances; the scale length that most closely approaches ours is that found for stars with Solar-type abundances, 1.28 kpc (but for  $R_{\text{gal}} > 8$  kpc).

In Figure 6, bottom, the behavior of the SFR profile as a function of  $R_{\text{gal}}$  is further analyzed by means of its cumulative. Although this curve is reminiscent of the SFR density profile shown in the top panel, it additionally accounts for the increasing area of the ring at increasing  $R_{\text{gal}}$ . For our

data we notice three most evident changes of slope in the cumulative at around 4 (marked steepening), 7 (getting shallower), and 10 kpc (flattening), respectively. We find that the 50%, 90%, and 99% of total SFR are achieved at  $R_{\text{gal}} = 5.8$ , 9.2, and 13.4 kpc, respectively. This means that, according to our results, half of the Galactic SFR comes from within the Molecular Ring, and just 1% from the far outer Galaxy ( $R_{\text{gal}} > 13.5$  kpc, according to the definition by Heyer et al. 1998).

### 3.3. Testing the Kennicutt-Schmidt relation

The SFR density profile computed in rings of  $R_{\text{gal}}$  and plotted in the top panel of Figure 6 can be also used for checking if the SFR in the Milky Way follows the Kennicutt-Schmidt (KS) law.

This is an empirical scaling relation (Schmidt 1959; Kennicutt 1998) generally found between star formation rate density  $\Sigma_{\text{SFR}}$  and mean gas (atomic + molecular) surface density  $\Sigma_{\text{gas}}$  in disk galaxies (the atomic and molecular gas density,  $\Sigma_{\text{H}_1}$  and  $\Sigma_{\text{H}_2}$ , respectively, can be also considered separately, see Bigiel et al. 2008; Kennicutt & Evans 2012). It is expressed by a power law such as

$$\Sigma_{\text{SFR}} \propto \Sigma_{\text{gas}}^n, \quad (3)$$

with  $n$  generally falling in the range 1 to 2, depending on the tracer used and the linear scales considered. In particular, the “classic” slope of Kennicutt (1998) is  $n = 1.40 \pm 0.15$ , with  $\Sigma_{\text{gas}}$  expressed in units of  $\text{M}_\odot \text{ pc}^{-2}$ . Finally, in the literature descriptions of  $\Sigma_{\text{SFR}}$  as a power law of the single atomic ( $\Sigma_{\text{H}_1}$ ), or molecular component ( $\Sigma_{\text{H}_2}$ ), respectively, can be also commonly found.

Whereas a vast literature is available about external galaxies following the KS relation (see, e.g., Kennicutt 1998; Miettinen et al. 2017; Orr et al. 2018, and references therein), this has been poorly tested for the Milky Way, also due to well understood intrinsic difficulties related to observing the Galaxy “from within”.

The KS relation for a set of regions in the Southern Milky Way was explored by Luna et al. (2006), who considered only  $\Sigma_{\text{H}_2}$  and found an exponent  $n = 1.2 \pm 0.2$ . Similarly, Sofue & Nakanishi (2017) found  $n = 1.12 \pm 0.05$  for a set of  $(\Sigma_{\text{SFR}}, \Sigma_{\text{H}_2})$  pairs obtained through binning the Galactic plane in  $0.2 \times 0.2$  kpc<sup>2</sup> boxes. No clear correlation was found, instead, between  $\Sigma_{\text{SFR}}$  and both  $\Sigma_{\text{H}_1}$  and  $\Sigma_{\text{gas}}$ . A steeper slope ( $3.7 \pm 1.6$ ), again considering only  $\Sigma_{\text{H}_2}$ , was found by Gutermuth et al. (2011). However, this value was based only on the analysis of a small sample of nearby star forming regions, which are not necessarily representative of the entire Galaxy.

Since in our case the available data set includes the entire Galactic plane, the approach we follow here is to plot the  $(\Sigma_{\text{SFR}}, \Sigma_{\text{H}_2})$  pairs azimuthally averaged in bins of Galactocentric radius (i.e. rings). This was done, for example, in

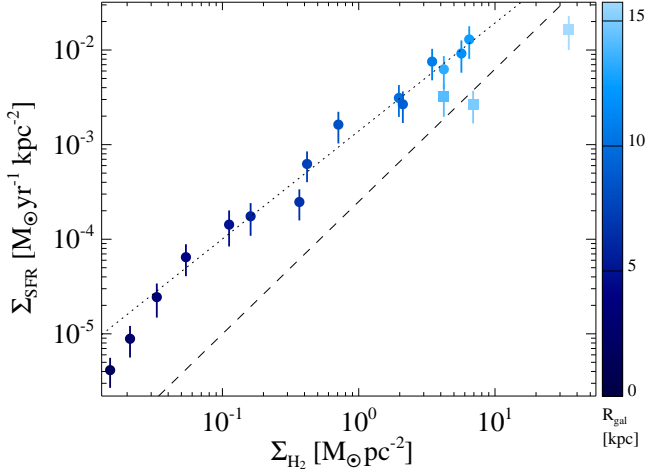


**Figure 7.** Star formation rate (SFR) estimated from the Hi-GAL observations versus the average molecular gas surface density (from [Miville-Deschénes et al. 2017](#)) in 1-kpc-wide concentric rings around the Galactic center whose central radius is indicated by the colors. The bins corresponding to  $R_{\text{gal}} \leq 3$  kpc, and  $R_{\text{gal}} > 3$  kpc are marked with square and circle symbols, respectively. The dotted and the dashed lines indicate the linear fit to the SFR estimates at  $R_{\text{gal}} \geq 3$  kpc (with slope  $n = 1.14 \pm 0.07$ ), and the KS relation ( $\Sigma_{\text{SFR}} = 2.5 \times 10^{-4} \Sigma_{\text{gas}}^{1.4}$ ), respectively.

[Boissier et al. \(2003\)](#), who found that the KS relation is satisfied in the range  $4 \leq R_{\text{gal}} \leq 15$  kpc with a slope of 2.06, and in [Misiriotis et al. \(2006\)](#), who obtained a slope of 2.18 across the entire range of  $R_{\text{gal}}$ .

To do that, for the  $x$  axis we use the molecular  $\Sigma_{\text{H}_2}$  averaged over Galactocentric bins of 1 kpc by [Miville-Deschénes et al. \(2017\)](#), starting from the CO survey assembled by [Dame et al. \(2001\)](#), and the atomic  $\Sigma_{\text{H}_1}$  from [Nakanishi & Sofue \(2016\)](#). Therefore, for consistency, we recalculated the SFR density in the same bins (which are twice wider than those used for Figure 6)<sup>3</sup>.

In Figure 7 the log-log plot of  $\Sigma_{\text{SFR}}$  vs  $\Sigma_{\text{H}_2}$  is shown. Differently from the plots built with the atomic and total gas density (see Appendix B), a linear trend can be recognized here, except for points corresponding to the innermost radii. For this reason, in the estimation of the linear fit, following the indication of [Boissier et al. \(2003\)](#), we do not consider the points corresponding to three first Galactocentric rings ( $R_{\text{gal}} \leq 3$  kpc). Notice that, as it can be seen in the bottom panel of Figure 6, the fraction of SFR contained within this radius correspond to only the 7% of the entire Milky Way SFR. From the fit to the remaining points, we obtain  $n = 1.14 \pm 0.07$ .

<sup>3</sup> See [Onodera et al. \(2010\)](#) and [Kruisssen & Longmore \(2014\)](#) for detailed discussions of minimum scales to be preserved while binning, to avoid incomplete sampling and consequent break down of star formation relations.

First of all, from the qualitative point of view, it is important to confirm that the largest part of the Milky Way disk follows a power-law behavior, testifying a direct and clear connection between the availability of molecular gas and the rate of its conversion into stars.

The slope  $n$  we found appears in good agreement with those derived by [Luna et al. \(2006\)](#) and [Sofue & Nakanishi \(2017\)](#), while it is shallower than those found by [Boissier et al. \(2003\)](#) and [Misiriotis et al. \(2006\)](#). Furthermore, we note the agreement of our result with that obtained by [Onodera et al. \(2010\)](#) for the M33 galaxy ( $n = 1.18 \pm 0.11$ ). The comparison with the classic slope of [Kennicutt \(1998\)](#), instead, makes little sense, since it refers to the total  $\Sigma_{\text{gas}}$ .

Actually, it is known that a variety of slopes is generally found for the KS relation (see, e.g., [Kennicutt & Evans 2012](#), and references therein). Furthermore, it is not difficult to figure out how varying some assumptions made in calculating the plotted variables can produce a change of the slope (even though preserving the global power-law behavior). For example, surface densities were computed by [Miville-Deschénes et al. \(2017\)](#) by converting CO to  $\text{H}_2$  by using the constant factor  $X_{\text{CO}} = 10^{20} \text{ cm}^{-2} (\text{K km s}^{-1})^{-1}$ . However, if an increasing trend of  $X_{\text{CO}}$  at increasing  $R_{\text{gal}}$  was adopted (e.g., [Nakanishi & Sofue 2006](#); [Pineda et al. 2013](#)), the plot in Figure 7 would get steeper (see also [Boissier et al. 2003](#)). Moreover, the masses used here as input for the SFR calculation were derived by [Elia et al. \(2021\)](#) by assuming a constant gas-to-dust ratio of 100. However, a possible increase of this ratio at increasing  $R_{\text{gal}}$  is suggested by [Giannetti et al. \(2017\)](#), and invoked by [Elia et al. \(2021\)](#) themselves to better explain the Galactocentric behavior of the surface density of Hi-GAL clumps. Taking into account such dependence would produce a flattening of our  $\Sigma_{\text{SFR}}$  vs  $\Sigma_{\text{H}_2}$  plot.

### 3.4. Face-on view of the Milky Way's SFR

Mapping the SFR in the Galactic plane as in Figure 5 offers the chance of comparing the local values of this observable with those of other quantities that can be mapped starting from the Hi-GAL clump distribution in the plane.

In our estimates, the SFR is the sum of the contributions from each protostellar clump, which is a function of its mass. In this respect, the spatial distribution of SFR in bins of  $[x, y]$  coordinates mirrors that of total mass of protostellar clumps in those bins. This total mass, in turn, does not necessarily depend on the number of protostellar clumps  $N_{\text{pro}}$  found

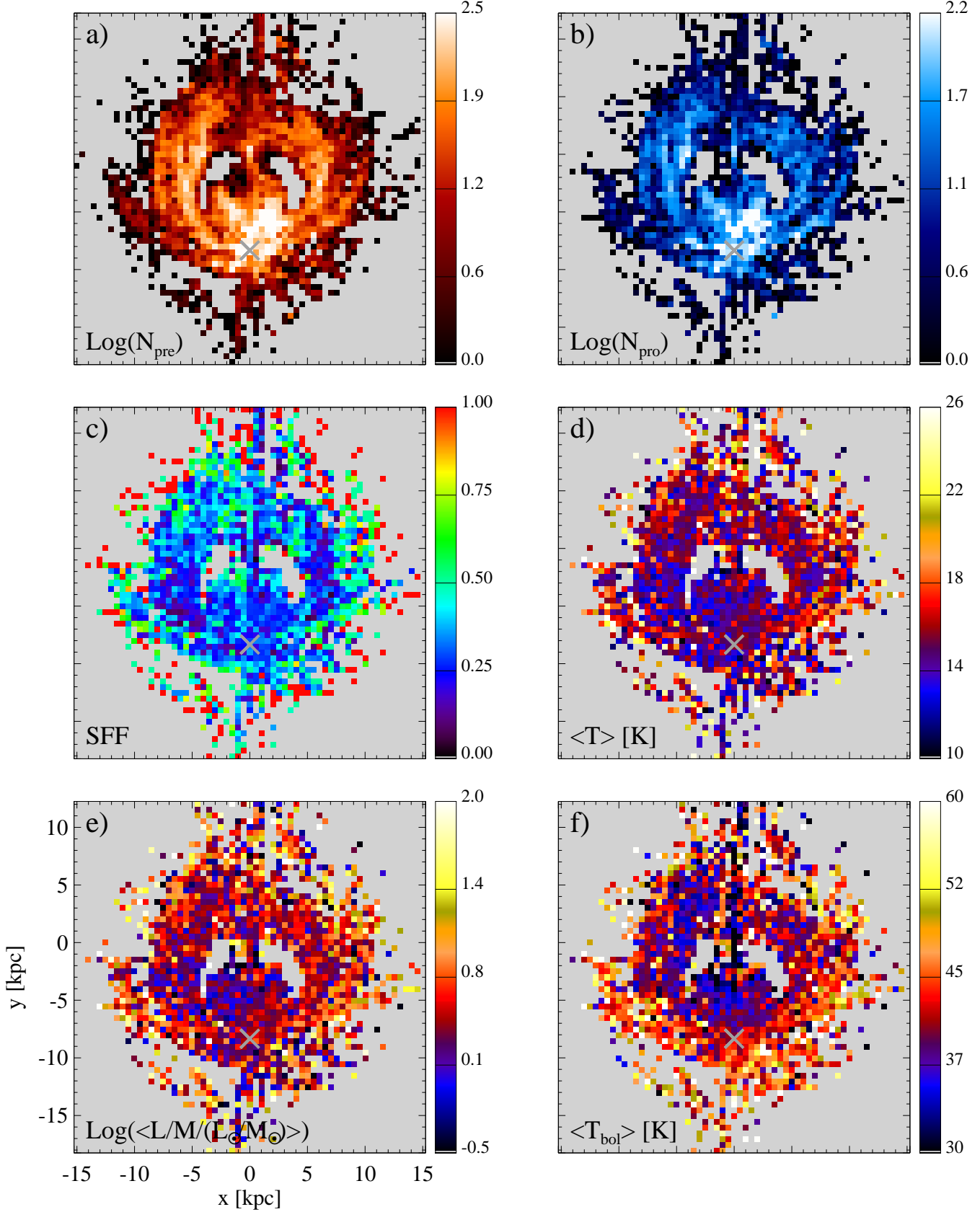


**Figure 8.** Face-on view of the Milky Way representing the following quantities derived (with the same spatial binning used for Figure 5) from the Hi-GAL observations: *a*) logarithm of number of pre-stellar Hi-GAL clumps per bin,  $N_{\text{pre}}$ ; *b*) logarithm of number of protostellar Hi-GAL clumps per bin,  $N_{\text{pro}}$ ; *c*) star formation fraction, SFF; *d*) median temperature (from modified black body fit) of protostellar clumps,  $\langle T \rangle$ ; *e*) median logarithm of luminosity-to-mass ratio normalized to the solar values,  $\langle (L/M)/(L_{\odot}/M_{\odot}) \rangle$ ; *f*) median bolometric temperature of protostellar clumps,  $\langle T_{\text{bol}} \rangle$ . In each panel, the [0,0] position corresponds to the Galactic center position, and the gray X symbol indicates the position of the Sun.

in each bin (shown in Figure 8, *b*)<sup>4</sup>, and does not depend at all on the number of pre-stellar clumps  $N_{\text{pre}}$  (shown in Figure 8, *a*). These two quantities were combined together by Ragan et al. (2016) to obtain the star formation fraction (hereafter SFF), defined as the ratio  $N_{\text{pro}} / (N_{\text{pre}} + N_{\text{pro}})$ . The relative populations of these two classes depend on their corresponding lifetimes, which in turn depend on the mass (Motte et al. 2010; Urquhart et al. 2014; Elia et al. 2021). In this respect, the local SFF is related not only to the overall evolutionary state of clumps in a given region, but also, indirectly, to their mass spectrum. Using Hi-GAL data, Ragan et al. (2016) highlighted a decreasing behavior of SFF as a function of the Galactocentric radius over the  $3.1 \text{ kpc} < R_{\text{gal}} < 8.6 \text{ kpc}$  range. This was confirmed by Elia et al. (2021), who however found a more scattered behavior just outside this range. This 1-D description of the SFF is further developed here in the 2-D mapping shown in the panel *c* of Figure 8, in which we can recognize the aforementioned decrease of this quantity at intermediate Galactocentric radii as a blueish ring-like area.

It makes sense to compare here the maps of SFR and SFF, since on the one hand they have no direct link a priori, and on the other hand this allows us to check whether locally the star formation rate is somehow correlated to the average evolutionary stage of the region. A bin-to-bin comparison between SFR and SFF is shown in panel *i* of Figure 9. Apparently, no correlation emerges from the plot, except for the fact that a small number of bins with very low SFF ( $\ll 1$ ) also exhibit relatively low SFR values.

As a further check of the absence of a trend with the average evolutionary stage of clumps in different parts of the disk, we also investigate the trend of the SFR versus the medians of meaningful evolutionary indicators for protostellar clumps, such as modified black body temperature  $T$ , bolometric luminosity over mass ratio  $L/M$ , and bolometric temperature  $T_{\text{bol}}$  (Cesaroni et al. 2015; Elia et al. 2017, 2021). Median values were evaluated for them in the same spatial bins of Figure 5, and displayed in Figure 8, panels *d*, *e*, and *f*, respectively.

For the median temperature and  $L/M$  ratio of protostellar clumps, Elia et al. (2021) did not find relevant variations in the 1-D profile as a function of  $R_{\text{gal}}$ , apart from an increase in the far outer Galaxy, but supported by poor statistics. On the contrary, the trend found for median  $T_{\text{bol}}$  is to slightly raise at increasing  $R_{\text{gal}}$ . This is what can be seen also in the 2-D view

provided in Figure 8. Therefore, the bin-to-bin comparison of quantities nearly constant with  $R_{\text{gal}}$  such as  $T$  and  $L_{\text{bol}}/M$  and an observable with a more complex spatial pattern (SFR) is expected to show no correlation between the two, as confirmed by Figure 9, panels *ii* and *iii*. A mild indication seems to be provided by bins with poor statistics (i.e. containing less than 20 clumps, so an even smaller number of protostellar ones), generally corresponding to large  $R_{\text{gal}}$ , for which a higher  $L/M$  but a small SFR (due to deficit of clumps) can be found. A similar, but clearer, behavior can be seen also considering the median  $T_{\text{bol}}$  (panel *iv*), essentially due to the increase of this observable with  $R_{\text{gal}}$ .

The large degree of scatter between the local SFR and median evolutionary indicators suggests that while the SFR, as it is calculated here, essentially depends on the local availability of mass, it is quite insensitive to the average evolutionary stage of clumps. In fact, it increases with the number of protostellar clumps and with their masses. Therefore, massive star forming regions surely provide a relevant contribution to the SFR of the Milky Way, however this does not seem to depend - once their mass is given - on an earlier or later mean evolutionary stage. This confirms the result found by Komugi et al. (2018) for M 33, namely the fact that the SFR is clearly correlated with the cloud density, in a somehow extended meaning of the KS relation, but not with the evolutionary stage.

### 3.5. SFR and spiral arm locations

In several portions of the spatial distribution of SFR density  $\Sigma_{\text{SFR}}$  in the Galactic plane shown in Figure 5 it is possible to recognize stretches of spiral arm features, similarly to what has been observed in external galaxies (Rebolledo et al. 2015; Elagali et al. 2019; Yu et al. 2021).

The SFR arm-like features are not much different from the pattern visible also in the distribution of protostellar clumps (Figure 8, panel *b*), i.e. the elements from which the SFR is computed. However, as already discussed in Elia et al. (2017, 2021), a relevant amount of clumps with “inter-arm” distances is also found, due to a large spread in velocities detected along many lines of sight of spectral surveys (Mège et al. 2021). Additionally, each different analytic spiral arm prescription available in the literature is able to successfully reproduce the observations over wide ranges of longitude, but can fail to fit observed arm-like features along other directions.

In Figure 5 we show, as an example, the four-arm prescription by Hou et al. (2009). It appears in good agreement with enhancements of our SFR density map along a significant portion of the Perseus arm; a good agreement is also found for the Norma and Carina-Sagittarius arms in the third quadrant, and for the Carina-Sagittarius and Crux-Scutum arms in the first octant of the fourth quadrant, respectively. Nev-

<sup>4</sup> Spatial distributions in panels *a* and *b* clearly appear asymmetric because at shorter heliocentric distances a larger number of sources (having relatively smaller physical sizes and masses) is detected. Conversely, at higher distances sources tend to appear blended in physically larger structures (Section 2.1). Since the SFR depends on the available mass (Section 2.2), the final appearance of the SFR density map in Figure 5 appears much more symmetric than that of source counts. Moreover, the selection bias with distance has to be taken into account; this is done in Appendix A.

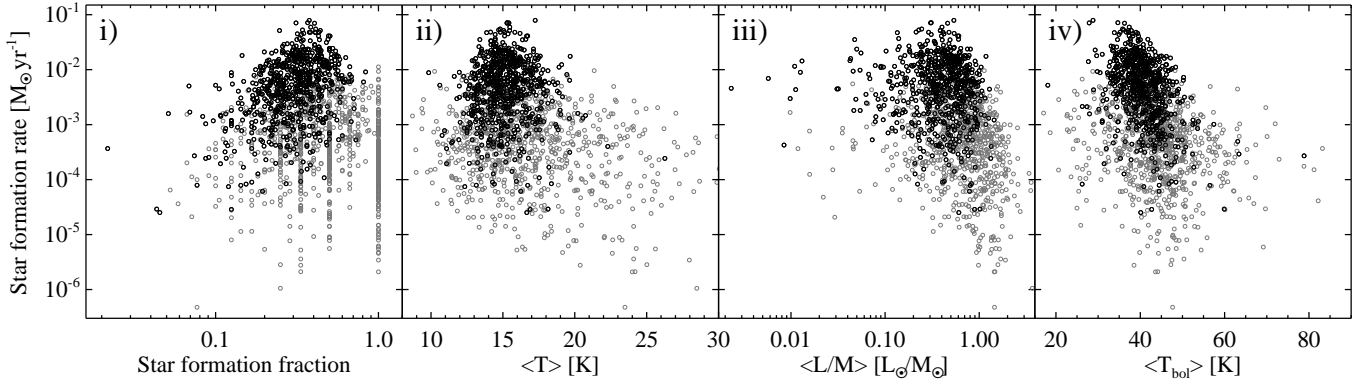


**Figure 9.** Star formation rate (SFR), evaluated in bins of 0.5 kpc in the  $[x, y]$  plane, as a function of star formation fraction (i), and medians of temperature (ii),  $L/M$  ratio (iii) and bolometric temperature (iv) of protostellar clumps, respectively, all calculated in the same spatial bins. In this respect, they represent a pixel-to-pixel plot Figure 5 vs panels c, d, e and f of Figure 8, respectively. Gray symbols correspond to bins with  $N_{\text{pro}} + N_{\text{pre}} < 20$ , considered statistically poor. In the leftmost panel, several of them give rise to vertical features corresponding to recurring values like  $N_{\text{pro}}/(N_{\text{pro}} + N_{\text{pre}}) = 1/1, 1/2, 1/3, 1/4$ , etc.).

ertheless, there are other regions with high SFR density, but not directly intersected by one of the displayed arms. All these aspects are mirrored in the distribution of the  $\Sigma_{\text{SFR}}$  values in Figure 5, if pixels closer than 0.5 kpc from a whatever spiral arm candidate plotted in the figure are considered separately from the remaining ones (Figure 10, top). The distribution of the “on-arm” pixels is visibly more left-skewed than the one of the “off-arm” pixels. In short, we observe a sufficiently clear spiral arm structure in the SFR spatial distribution, which elects spiral arms as preferential (although not unique) places for star formation activity in the Galaxy.

A similar spiral arm-like structure, on the contrary, is not seen in Figure 8 in the distributions of both SFF (panel c) and median evolutionary indicators as  $T$  (d),  $L_{\text{bol}}/M$  (e), and  $T_{\text{bol}}$  (f). Figure 10, middle, contains a comparison between the on-arm and off-arm distributions of SFF. These two distributions appear to be much less distinguishable than in the case of  $\Sigma_{\text{SFR}}$  (top panel). A similar behavior can be also seen for  $\langle L_{\text{bol}}/M \rangle$  (Figure 10, middle), taken as an example for the three considered evolutionary indicators.

These considerations reinforce the conclusions of Ragan et al. (2016) and Elia et al. (2021) about the role of spiral arms, i.e. that no significant differences in the mean evolutionary stage of star formation between spiral arms and inter-arm regions are found. The main difference between these two regions seems rather to consist in the larger amount of material available for star formation in the former than in the latter (see also Moore et al. 2012).

#### 4. SUMMARY

We used the information contained in the catalog of Hi-GAL clump physical properties to obtain a self-consistent estimate the Milky Way SFR. The main points to be summarized are:

- We extrapolated from the algorithm proposed by Veneziani et al. (2013) and Veneziani et al. (2017) an operative analytic prescription to obtain the contribution to the SFR from the mass of each far-infrared clump:  $\text{SFR}_{\text{clump}} = 5.6 \times 10^{-7} (M_{\text{clump}}/\text{M}_\odot)^{0.74} \text{ M}_\odot \text{ yr}^{-1}$ .
- Considering all clumps classified as protostellar (i.e. star forming) in the catalog and provided with a heliocentric distance, we obtain  $\text{SFR} = 1.7 \pm 0.6 \text{ M}_\odot \text{ yr}^{-1}$ .
- If we also take into account the contribution from the protostellar clumps without distance assignment, we estimate an additional contribution of  $0.22 \text{ M}_\odot \text{ yr}^{-1}$  to the global SFR, assuming that their distances follow the same distribution as the sources with known locations. This would lead to a final  $\text{SFR} = 2.0 \pm 0.7 \text{ M}_\odot \text{ yr}^{-1}$ . Also simulating the extreme case consisting in placing all those sources at  $d = 13$  kpc, the corrective term would not surpass  $0.57 \text{ M}_\odot \text{ yr}^{-1}$ .
- The profile of SFR surface density as a function of the Galactocentric radius  $R_{\text{gal}}$  is qualitatively similar to other results in the literature for the Milky Way and NGC 6946, and is consistent with most recent models (Evans et al. 2022). The absolute maximum is found in correspondence of the CMZ, and another local peak is found around  $R_{\text{gal}} = 5$  kpc, after which the logarithm of SFR density linearly decreases at increasing  $R_{\text{gal}}$ , with slope -0.28.
- Studying the cumulative of the SFR as a function of the Galactocentric radius, we find that 50% of the entire Milky Way SFR comes from within the so-called Molecular Ring, and 84% from within the Solar circle (inner Galaxy,  $R_{\text{gal}} < 8.34$  kpc). The outer Galaxy is

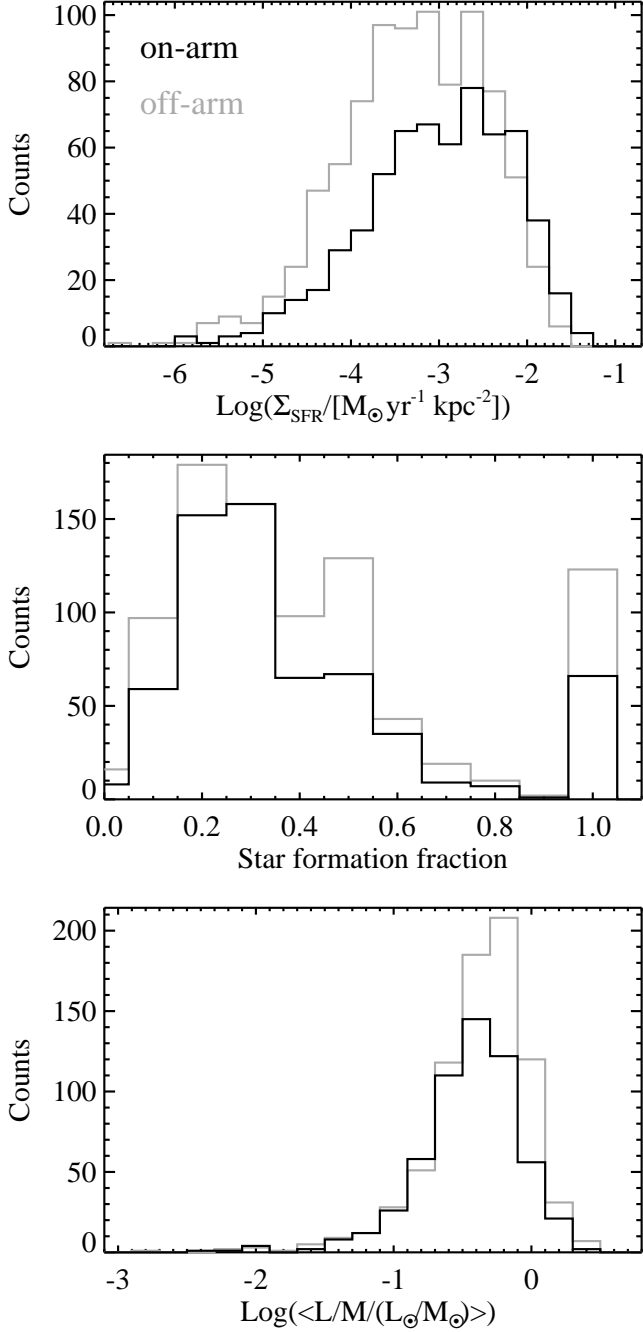


**Figure 10.** *Top:* histograms of logarithm of SFR density for pixels of the map in Figure 5, classified as on-arm (black) and off-arm (gray), based on the fact that their minimum distance from at least one of the spiral arms displayed in Figure 5 is shorter or longer than 0.5 kpc, respectively. *Middle:* the same as in the top panel, but for pixels of the map of SFF in Figure 8, panel *c*. *Bottom:* the same as in the previous panels, but for pixels of the map of  $\langle L_{\text{bol}}/M \rangle$  in Figure 8, panel *e*.

therefore responsible of 16% of total SFR and, in particular, the far outer Galaxy ( $R_{\text{gal}} > 13.5$  kpc) of 1%.

- The relation between SFR density and the molecular gas surface density Galactocentric profiles follows, for  $R_{\text{gal}} > 3$  kpc (containing the 93% of the entire Galactic SFR), a Kennicutt-Schmidt behavior, with slope  $n = 1.14 \pm 0.07$ .

- We find no significant trend relating the maps of SFR and those of the observables considered indicative of the mean local evolutionary stage of clumps. We conclude that the local SFR is determined by the amount of available mass rather than by the clump evolutionary stage.

- In the distribution of SFR across the Galactic plane, arm-like enhancements emerge over wide ranges of longitude. These enhancements are not seen in maps of the clump evolutionary indicators, suggesting that they are produced by source crowding within the arms.

<sup>1</sup> This research has received funding from the INAF Main-  
<sup>2</sup> stream Grant “The ultimate exploitation of the Hi-GAL  
<sup>3</sup> archive and ancillary infrared/mm data” (1.05.01.86.09), and  
<sup>4</sup> from the European Research Council synergy grant ECO-  
<sup>5</sup> GAL (855130). SL acknowledges support by the INAF PRIN  
<sup>6</sup> 2019 grant ONSET. AZ thanks the support of the Institut  
<sup>7</sup> Universitaire de France.

*Facilities:* Herschel

### A. EVALUATING THE COMPLETENESS OF THE TOTAL SFR ESTIMATE FOR THE MILKY WAY

Here we provide an estimate of the validity of the total SFR derived for the Milky Way in Section 2.2 in the light of possible incompleteness of the Hi-GAL catalog for large heliocentric distances.

Elia et al. (2017) showed how the mass completeness limit for Hi-GAL, based on the 350- $\mu$ m band flux, varies with source temperature and distance. For  $T = 16$  K, similar to the median temperature for Hi-GAL star forming clumps (Elia et al. 2021), a distance  $d = 10$  kpc, and a typical flux completeness limit of 5 Jy for the inner Galaxy (Molinari et al. 2016), the mass completeness limit amounts to  $\sim 90 M_{\odot}$ . One can therefore expect a shortage of detected clumps with mass lower than that, ignored in the SFR calculation. Here we give a quantitative discussion of this possible effect.

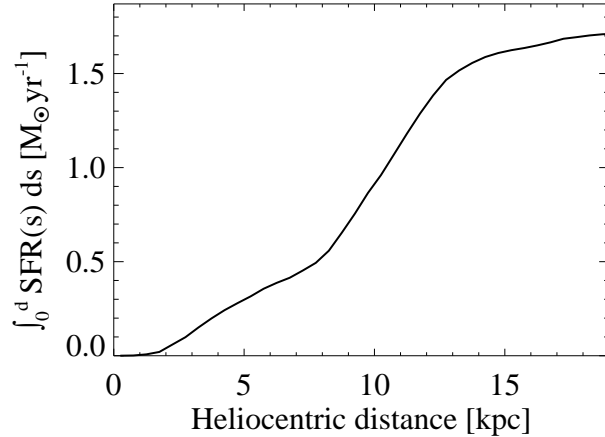


**Figure A1.** Cumulative SFR profile as a function of the heliocentric distance. Since the distance  $d$  appears as upper limit of integration, here the integration variable is called  $s$ .

First, we compute the cumulative SFR as a function of the distance. In Figure A1 a sharp change from a steeply positive to an almost horizontal slope is seen around  $d = 12$  kpc. The same can be affirmed, but in terms of source number, noting that around the same distance a decreasing trend is seen to start also in Figure 2. Such a change of slope can, in principle, be a combination of the true distribution of the SFR density in the plane and the selection effect due to distance we want to quantify. In the Hi-GAL catalog distances  $d > 12$  kpc are achieved by sources in the first and fourth quadrants<sup>5</sup> and the total SFR due to such sources is  $0.45 M_{\odot} \text{ yr}^{-1}$ .

Second, we evaluated the SFR from the symmetrical region on the opposite side of the Milky Way, i.e. we considered clumps (essentially located in the second and third quadrants) lying outside the circle centered on the symmetric point of the Sun with respect to the Galactic center ( $[x, y] = [0, +8.34]$  kpc) and with a radius of 12 kpc. The SFR from this area amounts to  $0.60 M_{\odot} \text{ yr}^{-1}$ , so that, in the rough assumption of a circular symmetry for the “true” SFR distribution in the  $[x, y]$  plane, the “missing SFR” due to incompleteness is comparable to the difference in SFRs measured from the two zones, namely  $0.15 M_{\odot} \text{ yr}^{-1}$ . The extent of this correction shows that the effect of the catalog incompleteness is not much strong, although not negligible: it should be added as a further term to the total estimate of  $1.7 M_{\odot} \text{ yr}^{-1}$  based on clumps provided with a distance estimate (Section 2.2), then representing a 8% correction to it.

To evaluate an analogous additional term for the SFR of  $2.0 M_{\odot} \text{ yr}^{-1}$ , estimated by involving also clumps with no distances (Section 2.2.1) is more complicated, because the distribution itself of known distances is involved in the calculation. However, assuming a 8% correction also in this case, the total Milky Way SFR would amount to  $2.13 M_{\odot} \text{ yr}^{-1}$ .

### B. TESTING THE KENNICUTT-SCHMIDT RELATION WITH ATOMIC GAS

To complete the discussion about the SFR vs gas density relation contained in Section 3.3, here we show the plots of  $\Sigma_{\text{SFR}}$  vs  $\Sigma_{\text{H}_1}$  (Figure B1, left) and  $\Sigma_{\text{gas}} = \Sigma_{\text{H}_1} + \Sigma_{\text{H}_2}$  (right), respectively, obtained using the Galactocentric profile of H<sub>I</sub> surface density of Nakanishi & Sofue (2016, their Figure 4).

<sup>5</sup> Notice that, since the relation between Galactocentric radius and heliocentric distance is  $R_{\text{GC}} = \sqrt{R_0^2 + d^2 + 2R_0 d \cos \ell}$ , sources placed at a same distance span a variety of Galactic locations, with the minimum  $R_{\text{GC}}$  achieved for  $\ell = 0^\circ$ .

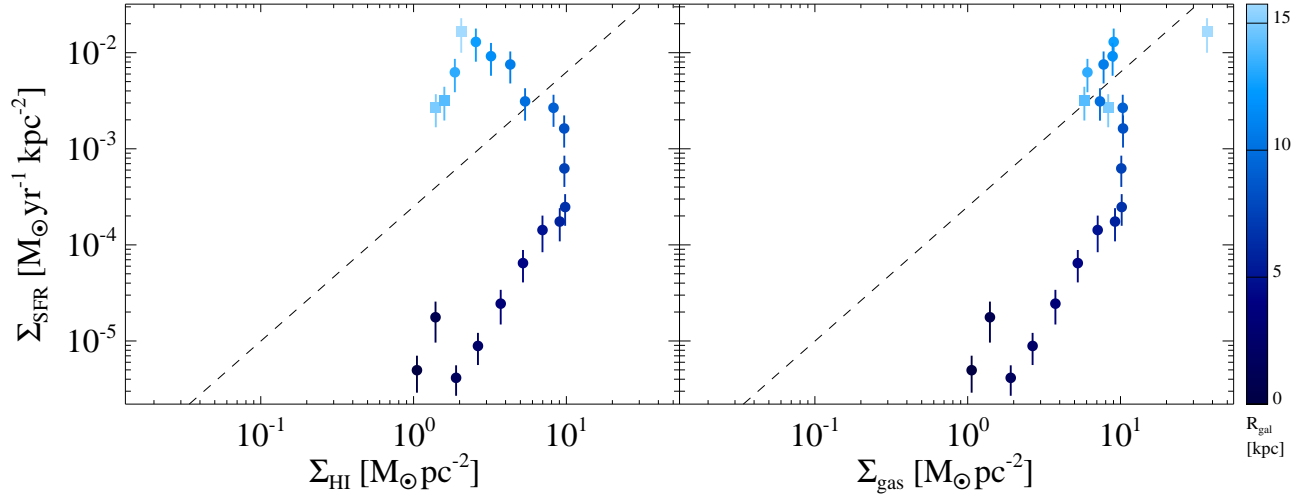


**Figure B1.** *Left:* the same as in Figure 7, but with atomic gas surface density on the  $x$  axis (from Nakanishi & Sofue 2016), instead of the molecular one. The KS relation is also plotted as a dashed line. *Right:* the same as in Figure 7 and in the left panel of this figure, but with total gas surface density on the  $x$  axis. In both panels the  $x$ -axis range has been kept identical to that of Figure 7, to facilitate comparison.

Comparing such profile with that of  $\Sigma_{\text{SFR}}$ , peaks for these two quantities are seen at very different values of  $R_{\text{GC}}$  (at  $\sim 10$  and  $\sim 5$  kpc, respectively), preventing a power-law relation between the two. Furthermore, for  $R_{\text{GC}} \lesssim 20$  kpc,  $\Sigma_{\text{HI}}$  varies only within one order of magnitude (namely between  $\sim 1$  and  $10 M_{\odot} \text{ pc}^{-2}$ ), so that the plot assumes an almost vertical appearance, as already highlighted by Sofue & Nakanishi (2017) and Bacchini et al. (2019). In this last work, in particular, it was shown how a power law behavior is recovered if the atomic+molecular gas volume density instead of the surface density is considered, which implies to take into account the increasing Galactic disk scale height at increasing  $R_{\text{GC}}$ .

Similar considerations can be formulated if one considers also the total gas surface density, which, as it can be seen in Miville-Deschénes et al. (2017), is dominated by the atomic component at  $R_{\text{GC}} \gtrsim 7$  kpc.

## REFERENCES

André, P., Men'shchikov, A., Bontemps, S., et al. 2010, A&A, 518, L102

Bacchini, C., Fraternali, F., Pezzulli, G., et al. 2019, A&A, 632, A127

Baldeschi, A., Molinari, S., Elia, D., Pezzuto, S., & Schisano, E. 2017a, MNRAS, 472, 1778

Baldeschi, A., Elia, D., Molinari, S., et al. 2017b, MNRAS, 466, 3682

Barnes, A. T., Longmore, S. N., Battersby, C., et al. 2017, MNRAS, 469, 2263

Barnes, P. J., Yonekura, Y., Fukui, Y., et al. 2011, ApJS, 196, 12

Bennett, C. L., Fixsen, D. J., Hinshaw, G., et al. 1994, ApJ, 434, 587

Bergin, E. A., & Tafalla, M. 2007, ARA&A, 45, 339

Bigiel, F., Leroy, A., Walter, F., et al. 2008, AJ, 136, 2846

Binney, J., Gerhard, O. E., Stark, A. A., Bally, J., & Uchida, K. I. 1991, MNRAS, 252, 210

Bland-Hawthorn, J., & Gerhard, O. 2016, ARA&A, 54, 529

Boardman, N., Zasowski, G., Newman, J. A., et al. 2020, MNRAS, 498, 4943

Boissier, S., Prantzos, N., Boselli, A., & Gavazzi, G. 2003, MNRAS, 346, 1215

Cesaroni, R., Pestalozzi, M., Beltrán, M. T., et al. 2015, A&A, 579, A71

Chiappini, C., Matteucci, F., & Romano, D. 2001, ApJ, 554, 1044

Chomiuk, L., & Povich, M. S. 2011, AJ, 142, 197

Crocker, R. M., Jones, D. I., Aharonian, F., et al. 2011, MNRAS, 413, 763

Cui, X.-Q., Zhao, Y.-H., Chu, Y.-Q., et al. 2012, Research in Astronomy and Astrophysics, 12, 1197

Dame, T. M., Hartmann, D., & Thaddeus, P. 2001, ApJ, 547, 792

Davies, B., Hoare, M. G., Lumsden, S. L., et al. 2011, MNRAS, 416, 972

Deng, L.-C., Newberg, H. J., Liu, C., et al. 2012, Research in Astronomy and Astrophysics, 12, 735

Diehl, R., Halloin, H., Kretschmer, K., et al. 2006, Nature, 439, 45

Dobbs, C. L., & Burkert, A. 2012, MNRAS, 421, 2940

Dunham, M. M., Crapsi, A., Evans, II, N. J., et al. 2008, ApJS, 179, 249

Elagali, A., Staveley-Smith, L., Rhee, J., et al. 2019, MNRAS, 487, 2797

Elia, D., Molinari, S., Fukui, Y., et al. 2013, *ApJ*, 772, 45

Elia, D., Molinari, S., Schisano, E., et al. 2017, *MNRAS*, 471, 100

Elia, D., Merello, M., Molinari, S., et al. 2021, *MNRAS*, 504, 2742

Ellsworth-Bowers, T. P., Rosolowsky, E., Glenn, J., et al. 2015, *ApJ*, 799, 29

Evans, Neal J., I., Heyer, M., Miville-Deschénes, M.-A., Nguyen-Luong, Q., & Merello, M. 2021, *ApJ*, 920, 126

Evans, N. J., Kim, J.-G., & Ostriker, E. C. 2022, *ApJL*, 929, L18

Fraser-McKelvie, A., Merrifield, M., & Aragón-Salamanca, A. 2019, *MNRAS*, 489, 5030

Gaia Collaboration, Brown, A. G. A., Vallenari, A., et al. 2018, *A&A*, 616, A1

Giannetti, A., Leurini, S., König, C., et al. 2017, *A&A*, 606, L12

Giannini, T., Elia, D., Lorenzetti, D., et al. 2012, *A&A*, 539, A156

Griffin, M. J., Abergel, A., Abreu, A., et al. 2010, *A&A*, 518, L3

Guesten, R., & Mezger, P. G. 1982, *Vistas in Astronomy*, 26, 159

Gutermuth, R. A., Pipher, J. L., Megeath, S. T., et al. 2011, *ApJ*, 739, 84

Heyer, M. H., Brunt, C., Snell, R. L., et al. 1998, *ApJS*, 115, 241

Hou, L. G., Han, J. L., & Shi, W. B. 2009, *A&A*, 499, 473

Immer, K., Schuller, F., Omont, A., & Menten, K. M. 2012, *A&A*, 537, A121

Jackson, J. M., Contreras, Y., Rathborne, J. M., et al. 2018, *ApJ*, 869, 102

Kennicutt, Robert C., J. 1998, *ApJ*, 498, 541

Kennicutt, Robert C., J., Hao, C.-N., Calzetti, D., et al. 2009, *ApJ*, 703, 1672

Kennicutt, R. C., & Evans, N. J. 2012, *ARA&A*, 50, 531

Koepferl, C. M., Robitaille, T. P., Morales, E. F. E., & Johnston, K. G. 2015, *ApJ*, 799, 53

Komugi, S., Miura, R. E., Kuno, N., & Tosaki, T. 2018, *PASJ*, 70, 48

Kroupa, P., & Weidner, C. 2003, *ApJ*, 598, 1076

Kruijssen, J. M. D., & Longmore, S. N. 2014, *MNRAS*, 439, 3239

Krumholz, M. R. 2014, *PhR*, 539, 49

Krumholz, M. R., & McKee, C. F. 2005, *ApJ*, 630, 250

Lada, C. J., Lombardi, M., & Alves, J. F. 2010, *ApJ*, 724, 687

Larson, R. B. 1981, *MNRAS*, 194, 809

Lee, E. J., Miville-Deschénes, M.-A., & Murray, N. W. 2016, *ApJ*, 833, 229

Li, Y., Calzetti, D., Kennicutt, R. C., et al. 2010, *ApJ*, 725, 677

Li, Z., Gerhard, O., Shen, J., Portail, M., & Wegg, C. 2016, *ApJ*, 824, 13

Lian, J., Thomas, D., Maraston, C., et al. 2018, *MNRAS*, 476, 3883

Licquia, T. C., & Newman, J. A. 2015, *ApJ*, 806, 96

Lindgren, L., Hernández, J., Bombrun, A., et al. 2018, *A&A*, 616, A2

Logroño-García, R., Vilella-Rojo, G., López-Sanjuan, C., et al. 2019, *A&A*, 622, A180

Longmore, S. N., Bally, J., Testi, L., et al. 2013, *MNRAS*, 429, 987

Luna, A., Bronfman, L., Carrasco, L., & May, J. 2006, *ApJ*, 641, 938

McKee, C. F., & Ostriker, E. C. 2007, *ARA&A*, 45, 565

McKee, C. F., & Williams, J. P. 1997, *ApJ*, 476, 144

Mège, P., Russeil, D., Zavagno, A., et al. 2021, *A&A*, 646, A74

Mezger, P. G. 1987, in *Starbursts and Galaxy Evolution*, ed. T. X. Thuan, T. Montmerle, & J. Tran Thanh van, 3–18

Miettinen, O., Delvecchio, I., Smolčić, V., et al. 2017, *A&A*, 602, L9

Misiriotis, A., Xilouris, E. M., Papamastorakis, J., Boumis, P., & Goudis, C. D. 2006, *A&A*, 459, 113

Miville-Deschénes, M.-A., Murray, N., & Lee, E. J. 2017, *ApJ*, 834, 57

Molinari, S., Pezzuto, S., Cesaroni, R., et al. 2008, *A&A*, 481, 345

Molinari, S., Schisano, E., Faustini, F., et al. 2011, *A&A*, 530, A133

Molinari, S., Swinney, B., Bally, J., et al. 2010, *PASP*, 122, 314

Molinari, S., Schisano, E., Elia, D., et al. 2016, *A&A*, 591, A149

Moore, T. J. T., Urquhart, J. S., Morgan, L. K., & Thompson, M. A. 2012, *MNRAS*, 426, 701

Motte, F., Zavagno, A., Bontemps, S., et al. 2010, *A&A*, 518, L77

Murray, N., & Rahman, M. 2010, *ApJ*, 709, 424

Mutch, S. J., Croton, D. J., & Poole, G. B. 2011, *ApJ*, 736, 84

Nakanishi, H., & Sofue, Y. 2006, *PASJ*, 58, 847

—. 2016, *PASJ*, 68, 5

Noriega-Crespo, A. 2013, in *Astrophysics and Space Science Proceedings*, Vol. 34, *Cosmic Rays in Star-Forming Environments*, ed. D. F. Torres & O. Reimer, 29

Onodera, S., Kuno, N., Tosaki, T., et al. 2010, *ApJL*, 722, L127

Orr, M. E., Hayward, C. C., Hopkins, P. F., et al. 2018, *MNRAS*, 478, 3653

Pilbratt, G. L., Riedinger, J. R., Passvogel, T., et al. 2010, *A&A*, 518, L1

Pineda, J. L., Langer, W. D., Velusamy, T., & Goldsmith, P. F. 2013, *A&A*, 554, A103

Poglitsch, A., Waelkens, C., Geis, N., et al. 2010, *A&A*, 518, L2

Portinari, L., & Chiosi, C. 1999, *A&A*, 350, 827

Ragan, S. E., Moore, T. J. T., Eden, D. J., et al. 2016, *MNRAS*, 462, 3123

Rebolledo, D., Wong, T., Xue, R., et al. 2015, *ApJ*, 808, 99

Reed, B. C. 2005, *AJ*, 130, 1652

Robitaille, T. P., & Whitney, B. A. 2010, *ApJL*, 710, L11

Roman-Duval, J., Heyer, M., Brunt, C. M., et al. 2016, *ApJ*, 818, 144

Russeil, D., Zavagno, A., Mège, P., et al. 2017, *A&A*, 601, L5

Schmidt, M. 1959, *ApJ*, 129, 243

Schroba, A., Leroy, A. K., Walter, F., et al. 2011, *AJ*, 142, 37

Smith, L. F., Biermann, P., & Mezger, P. G. 1978, *A&A*, 66, 65

Sofue, Y., & Nakanishi, H. 2017, *PASJ*, 69, 19

Soler, J. D., Miville-Deschénes, M. A., Molinari, S., et al. 2022, *A&A*, 662, A96

Traficante, A., Fuller, G. A., Billot, N., et al. 2017, *MNRAS*, 470, 3882

Urquhart, J. S., Moore, T. J. T., Csengeri, T., et al. 2014, *MNRAS*, 443, 1555

Veneziani, M., Elia, D., Noriega-Crespo, A., et al. 2013, *A&A*, 549, A130

Veneziani, M., Schisano, E., Elia, D., et al. 2017, *A&A*, 599, A7

Voskes, T., & Butler Burton, W. 2006, arXiv e-prints, astro

Westerhout, G. 1957, *BAN*, 13, 201

Xiang, M., Shi, J., Liu, X., et al. 2018, *ApJS*, 237, 33

Yu, S.-Y., Ho, L. C., & Wang, J. 2021, *ApJ*, 917, 88

Yusef-Zadeh, F., Hewitt, J. W., Arendt, R. G., et al. 2009, *ApJ*, 702, 178